# **Title:** Assessment of Two Recent Hot Dry Rock Thermal Energy Production Projects

Balnur Mindygaliyeva[a], Ozan Uzun[a], Kaveh Amini[a], Hossein Kazemi[a], and William Fleckenstein[a]

[a] *Department of Petroleum Engineering, Colorado School of Mines, Golden, CO 80401, USA*

ARTICLE INFO

*Keywords:*
Geothermal energy
Enhanced geothermal system (EGS)
Hydrothermal (HT)
Hot dry rock (HDR)
Well stimulation
Plug-and-perf
GeoThermOPTIMAL
Porosity
Permeability
Dual porosity (DP)
Discrete fracture network (DFN)
Heat transfer rate
Pressure falloff test
Pressure transient analysis (PTA)
Rate transient analysis (RTA)

**ABSTRACT**

**Geothermal energy** is heat within the Earth. It is an abundant, renewable energy source because heat is continuously produced inside the Earth. There are two types of geothermal reservoirs. The first type, the **hydrothermal (HT) reservoirs**, are subsurface porous and permeable hot rocks saturated with mobile hot water that can be withdrawn to the surface via production wells for electricity generation without any major reservoir stimulation. The second type consists of **hot dry rock (HDR) systems** where the rock has very low permeabilities and does not contain water; thus, requiring formation stimulation to generate permeability and injection of water to permeate the rock. In this paper, we present analyses of laboratory and field data indicating that the current two-well, injection-production system, connected with multiple hydraulic fractures, is the most promising method for extracting heat from HDR systems to generate electricity given the abundance of HDR systems in the Earth's crust. The current two-well system could be expanded to a three-well system consisting of one injection well and two symmetric producing wells connected with hydraulic fractures. To improve economics, we advocate field test of a newly designed well stimulation technique, the **GeoThermOPTIMAL,** as a potential cost-effective well stimulation technique than the common **plug-and-perf** stimulation techniques.

In this paper, we first present an analysis of the post-fracturing flow data obtained from a hot dry rock (HDR) geothermal injection well at the **Utah FORGE** enhanced geothermal system (EGS) research field site. The site is adjacent to the **Roosevelt hydrothermal (HT)** field. The objective of the study is to assess the effectiveness of well stimulation in extracting heat from the low-permeability, hot dry granitoid rock in the Utah FORGE research site. The study includes interpreting pressure falloff data obtained during the well stimulation process and employing laboratory-measured core data as a major input in the interpretation of the field falloff data. As a confirmation of the robustness of our analysis in Utah FORGE, we review and analyze the flow test results published for an injection-production doublet at the **Blue Mountain EGS** commercial site in Nevada. From the analyses of these two field tests, we have concluded that the interpretation and findings of the Blue Mountain EGS pilot test are consistent with the interpretation and findings from the Utah FORGE field research project test results.

In summary, our engineering assessments began with laboratory experiments conducted on various core samples, including those from a granite outcrop and the Utah FORGE geothermal reservoir. These experiments aimed to measure key parameters such as matrix and fracture permeabilities, and porosities. These data served as guides and inputs for analytical and numerical solutions used to match the field pressure response of the geothermal wells. While we did not have core samples from the Blue Mountain EGS wells, we successfully applied the Utah FORGE analysis approach to the Blue Mountain site with cautious optimism.

## 1. Introduction

Geothermal energy is the heat within the Earth, and it holds immense promise as a renewable source of electric power generation. This energy is continuously replenished by heat flow from inside the Earth into the Earth's crust. This paper assesses two recent energy production projects in hot dry rock formations in the western U.S.

Geothermal energy encompasses the limited hydrothermal (HT) conventional reservoirs and the more extensive hot dry rock (HDR) unconventional formations available worldwide. While conventional hydrothermal resources have played a vital role in various applications in the U.S. and around the world, their utilization is constrained by smaller geographic sites compared to the hot dry rock sources. The enhanced geothermal system (EGS) refers to the technologies that enhance or create geothermal resources in hot dry rock formations by creating permeable fracture networks, injecting cold water through an injection well into the fracture network and producing the heated water from the same well or preferably from a production well. The heated water is flashed into steam at the surface to generate electric power in a power plant.

The evolving EGS techniques and field tests underscore their considerable long-term potential (Tester et al., 2006; EIA, 2023). The appeal of geothermal energy lies in its ability to provide a consistent, dependable power source with minimal greenhouse gas emissions. Two recent studies have highlighted the colossal thermal energy reservoirs size beneath the Earth's surface which provides an opportunity to meet a significant portion of the world's energy demands while mitigating environmental impacts (DiPippo, 2005; Tester et al., 2006).

Hydrothermal (HT) reservoirs encompass porous, permeable, hot rocks, saturated with mobile hot water readily extractable through production wells for electricity generation without significant reservoir stimulation. The hydrothermal reservoirs form as hot water or steam is trapped in porous and fractured rocks beneath a relatively impermeable caprock layer, showcasing a natural heating phenomenon (U.S. Department of Energy, 2012). Well-known cases include the **Roosevelt Blundell hydrothermal** power plant in Utah, **Blue Mountain hydrothermal** reservoir in Nevada (Casteel et al., 2010), and the **California Geysers** (McLaughlin and Donnelly-Nolan, 1981), recognized as the world's largest hydrothermal field.

In contrast to hydrothermal reservoirs, hot dry rock (HDR) systems feature rocks with minimal permeabilities, necessitating hydraulic fracturing for fluid conductivity. This artificial stimulation enables circulating water in the stimulated rock fractures; thus, facilitating heat extraction from fractured surfaces. Notable examples of HDR systems include the **Utah FORGE EGS project** (Allis and Moore, 2019) and the **Blue Mountain EGS project** in Nevada (Norbeck et al., 2023). HDR systems represent a very large energy source with temperatures ranging from 150°C to 650°C, buried at depths of 3-10 km. The HDR geothermal sources consist of dense, high-temperature rock masses with limited or no liquid content. The immense thermal energy potential of HDR formations is estimated to be 30 times greater than the total amount of fossil energy, with a total heat storage capacity that can reach $2.52 \times 10^{25}$ J[1] in China, underscoring their significance (Zhang et al., 2018).

## 2. Utah FORGE EGS

The Utah FORGE EGS field research project consisted of drilling and completing a pair of parallel injection-production wells within the Utah FORGE area (**Fig. 1** and **Fig. 2**). The wells were drilled vertically to a depth of about 7,000 feet and slanted at 37 degrees with respect to the horizontal plane to a vertical depth of about 10,000 feet in a hot dry rock (HDR) formation (Moore et al., 2020). This HDR formation has remarkably low matrix permeability of about 0.001 mD and porosity of 0.01 without the presence of any mobile hot brine. As depicted in **Fig. 1a** and **Fig. 2**, the trajectory of the injector 16A(78)-32 and producer 16B(78)-32 were designed for connection by a sequence of hydraulic fractures (HF) (Kumar and Ghassemi, 2019). By April 2022, three hydraulic fractures had been initiated in the injection well, with the production well 16B(78)-32 completed in summer of 2023 approximately 300 feet parallel to the injection well 16A(78)-32 (Allis and Moore, 2019). Each hydraulic

[1] 1 kWh = 3.6 x 106 Joules = 3412.14 BTU

fracture was estimated to have two parallel surface areas of approximately 660 feet in diameter based on microseismic measurements (Nadimi et al., 2020) with the sole purpose to extract heat via injection and circulation of water. The hydraulic fracture surface areas are also connected to a swarm of stimulated micro- and macro-fracture systems in the rock volume between the hydraulic fractures. While the intrinsic permeability and interconnectivity of micro- and macro-fractures is extremely difficult to quantify, we believe we can calculate an effective permeability for the assemblage. It is anticipated that a portion of both pre-existing and newly generated fractures would direct part of the injected water into the stimulated volume between the hydraulic fractures and subsequently into the HDR matrix (Hill, 2021; Balnur Mindygaliyeva et al., 2023).

The geological complexity of Utah's south-central region is characterized by Quaternary volcanic activity, resulting in remarkably high surface heat flux levels that render it an attractive prospect for geothermal projects (Wells et al., 2022). Another noteworthy feature is the presence of extensional faulting, exemplified by the prominent Opal Mound fault, depicted in **Fig. 1b**. This fault, dipping eastward, acts as a hydrological barrier, impeding the lateral movement of hydrothermal fluids. To the east of this fault lies the **Roosevelt Hot Springs (RHS)** (Allis and Moore, 2019), a highly permeable hydrothermal geothermal system. Within the RHS, the groundwater primarily consists of mineral-rich thermal waters that predominantly flow northwestward and westward through a shallow, unconfined aquifer. The FORGE enhanced geothermal system (EGS) is strategically situated 5 kilometers west of the RHS, as indicated by the red polygon in **Fig. 1b**. The underlying geological formations at the FORGE site include Precambrian gneiss and Tertiary pluton, commonly referred to as granitoid (Nadimi et al., 2020; Simmons et al., 2016). A cross-sectional view of the FORGE site is shown in **Fig. 1d**, extending in a northwest-southeast direction. It not only illustrates the geological stratigraphy but also indicates temperature variations (isotherms) inferred from well measurements, with higher temperatures prevailing in the deeper western region (Xing et al., 2020).

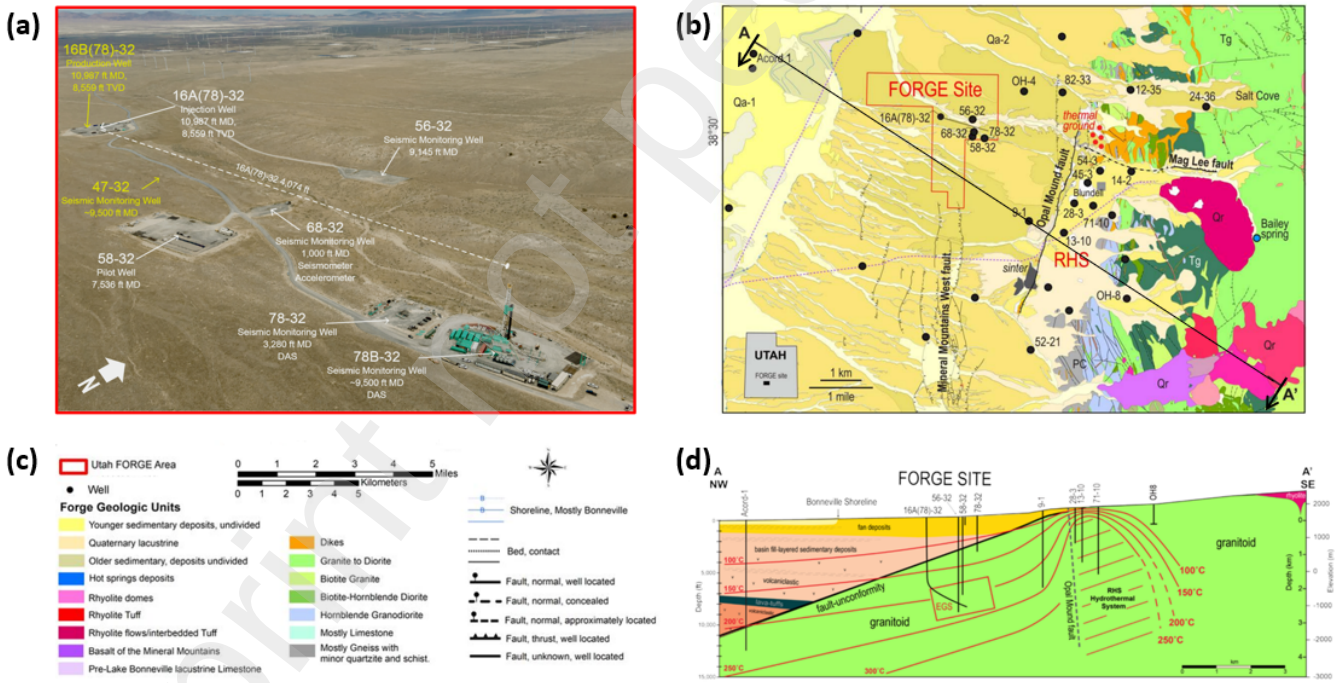


**Fig. 1.** (a) An aerial perspective from the northwest showcasing the Utah FORGE site, featuring the horizontal trajectory of injector well 16A(78)-32, the surface location of producer well 16B(78)-32, and the positions of drill pads for tool testing and seismic monitoring (Hill, 2021); (b) An illustrative geologic map delineating the FORGE site and its surrounding area (Geology, 2022); (c) Geologic symbols specific to the FORGE project (Geology, 2022); (d) A geologic map presenting a cross-sectional view from northwest to southeast of the FORGE Utah site, highlighting stratigraphy, structure, and thermal regimes (adapted from Kirby et al., 2018).

EGS systems aim to establish reservoirs by applying technologies initially developed for unconventional reservoir stimulation. These systems involve injecting fluids into enhanced reservoirs to capture and harness heat. Utilizing horizontal wells presents an opportunity to construct extensive reservoir systems with improved capabilities, enabling the efficient extraction of substantial heat for various applications (Fleckenstein et al., 2022, 2023a).

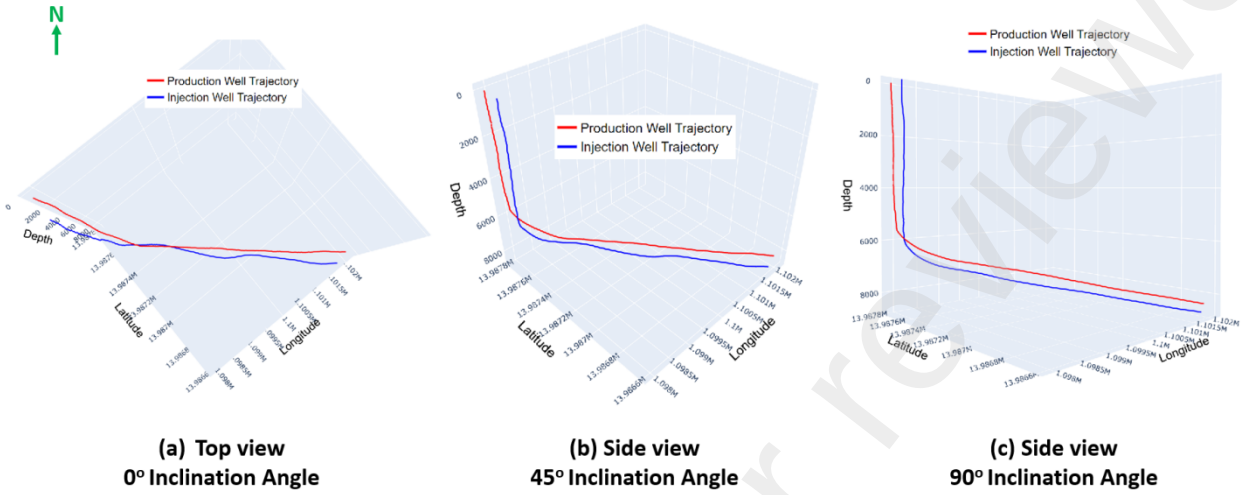


**Fig. 2.** Utah FORGE Injection-Production Wells' Directional Profiles: Wells 16A(78)-32 and 16B(78)-32 depicted facing north using geospatial coordinates: (a) top view with 0° inclination angle, (b) side view with 45° inclination angle, and (c) side view with 90° inclination angle (Source: McLennan et al., 2023, 2021).

### *2.1 Experimental Procedure*

Our experiments aimed to measure the permeability and porosity of granitoid cores obtained from both the FORGE site and an outcrop granite from a location unrelated to FORGE. Leveraging an automated core measurement instrument (Jones, 1972), we conducted these measurements both prior to and following the fracturing of the cores into halves. This allowed us to assess the matrix permeability and porosities of the cores in their intact and fractured states. The instrument facilitated these measurements by calculating porosity and permeability of the rock samples at specified confining stress levels within the range of 500-9800 psi. Programmed to utilize Boyle's Law, the instrument computed pore volume (PV) and porosity for samples falling within the PV range of 0.02—25 $cm^3$ and permeability range of 0.001 micro-Darcy to 5 Darcy. Notably, the instrument is unable to measure permeability and porosity for ultra-tight matrices (Cho, 2012). The application of confining stress on the cores was achieved by injecting nitrogen gas into a surrounding sleeve under biaxial loading, while helium gas was injected into the core at a pressure of 245 psi for flow measurement.

In our initial experiments, we focused on an outcrop granite sample, dividing it into two core plugs, each measuring 1-1/2 inch in diameter by 2 inches in length, meeting the instrument's size requirements. Prior to fracturing, we measured the porosity and permeability of one of the core plugs. The core underwent a net confining stress of 1755 psi and a pore pressure of 245 psi. Subsequently, we induced a single fracture along the long axis of each core using two different methods. The first method involved cutting the granite core sample (referred to as Granite Core 1, GC1) using a saw, as illustrated in **Fig. 3**.

For an alternate approach, we utilized a Material Testing System (MTS) apparatus to induce fractures in the core. This was achieved by gradually applying force on the cylindrical surface of the core. The core used for this method was labeled Granite Core 2, GC2, as depicted in **Fig. 4**.

Our observations indicated that the fracture generated in sample GC2 (**Fig. 4: d and e**) closely resembled natural micro-fractures, presenting a more accurate representation compared to the fracture in sample GC1 (**Fig. 3: d and e**). To ensure a successful experiment using the automated core measurement apparatus (CMS-300™), efforts were made to maintain

the integrity of the core halves. This was achieved by securely wrapping each sample with tape. For sample GC1 (**Fig. 3**), some loss of rock grains in the radial direction was observed; consequently, it was wrapped with polyvinyl chloride (PVC) tape to restore the correct diameter dimension necessary for the apparatus. On the other hand, there were no issues with the post-fracture diameter of sample GC2 (**Fig. 4**); nonetheless, Teflon tape was employed to hold the core halves together. Subsequently, we proceeded to measure the porosity and permeability of the fractured cores under identical confining stress conditions—1755 psi and 245 psi of pore pressure.

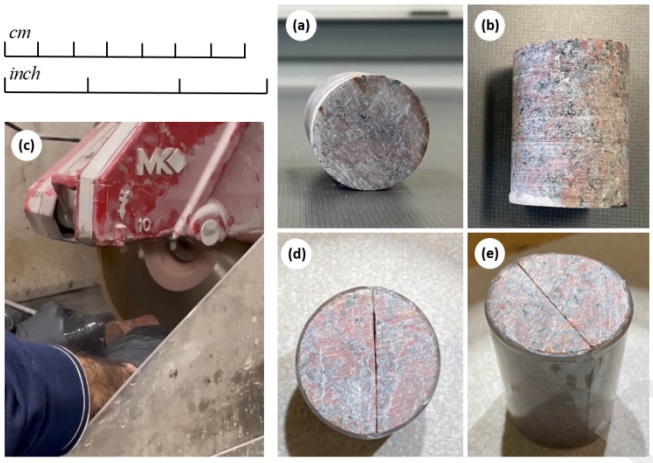


**Fig. 3.** Granite sample GC1 depicted in: (a) a top view and (b) a side view before fracturing (images adhere to the scale on the left); (c) the process of halving the core using a saw to induce a fracture; (d) a top view and (e) a side view of the fractured core, enveloped in PVC tape to maintain core integrity.

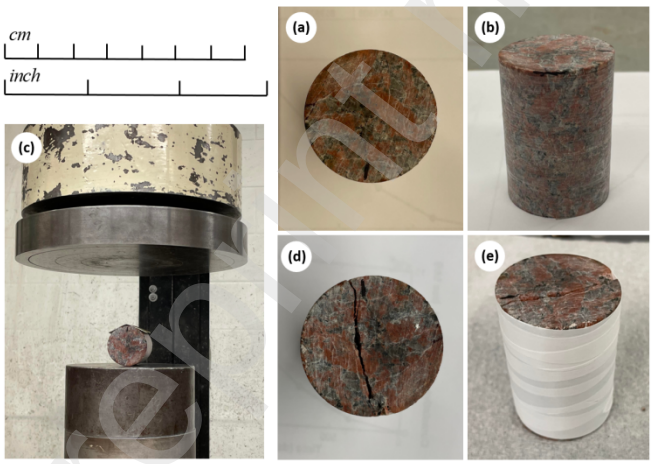


**Fig. 4.** Granite sample GC2 illustrated in: (a) a top view and (b) a side view before fracturing (the images adhere to the scale on the left); (c) the core positioned within the MTS machine to induce a fracture; (d) a top view and (e) a side view of the fractured core, enveloped in Teflon tape to maintain core integrity.

The fracturing procedures illustrated in **Fig. 3c** and **4c** were executed on two granitoid cores sourced from the Utah FORGE injection well 16A(78)-32. Specifically, the horizontal core A4-9H (**Fig. 5b**) originated from a measured depth (MD) of 10981.9 ft, while the vertical core A3-8V (**Fig. 6b**) was retrieved from a measured depth of 10955.9 ft. The permeability and porosity of the horizontal core A4-9H were initially measured prior to fracturing using our core measurement apparatus. This was done at net confining stresses of 1255 psi, 1755 psi, and 2755 psi, accompanied by a pore pressure of 245 psi. However, the apparatus couldn't furnish measurements for the vertical core A3-8V under a net confining stress of 2755 psi. Consequently, flow property assessments for this core before fracturing were conducted at net confining stresses of 1255 psi, 1555 psi, 1755 psi, and 2255 psi. These measurements were also repeated in reverse order. Subsequently, the core A4-9H (**Fig. 5b**) was successfully sectioned using a saw, and permeability measurements were carried out as previously described.

When attempting to induce a fracture in the vertical core, A3-8V, as shown in **Fig. 6b**, using the MTS machine, and maintaining a controlled force rate, the core disintegrated, thwarting the fracture creation process!

Despite encountering experimental challenges, we successfully acquired reliable measured results from the core experiments. These results will serve as crucial input data for our mathematical modeling and subsequent analysis of the pressure falloff tests conducted in the Utah FORGE project.

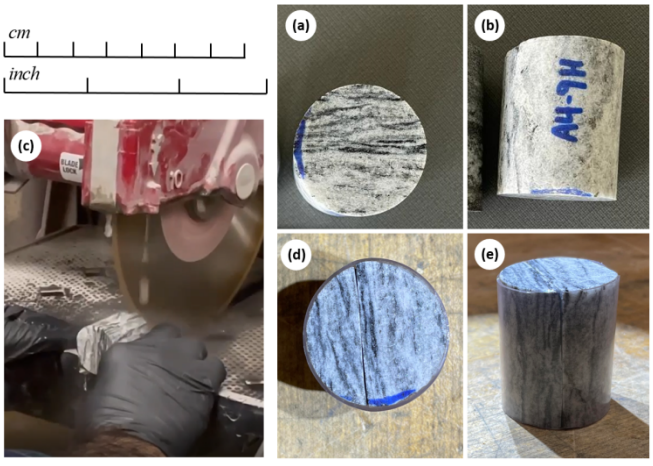


**Fig. 5.** Horizontal sample A4-9H from FORGE portrayed in: (a) a top view and (b) a side view before fracturing (images adhere to the scale on the left); (c) the process of halving the core using a saw to induce a fracture; (d) a top view and (e) a side view of the fractured core, encased in PVC tape to maintain core integrity.

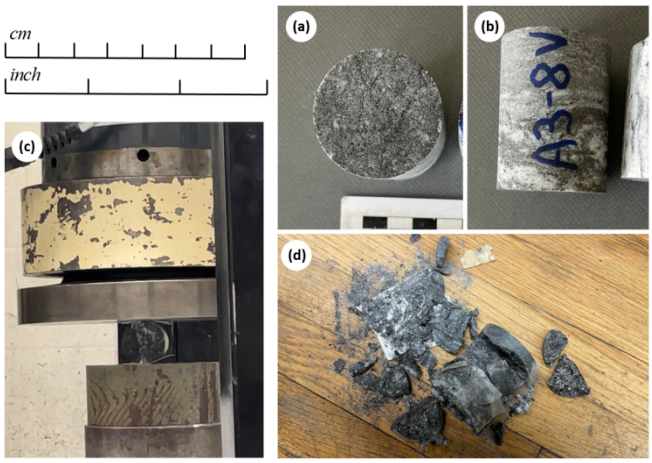


**Fig. 6.** Vertical sample A3-8V from FORGE portrayed in: (a) a top view and (b) a side view before fracturing (images adhere to the scale on the left); (c) the core positioned within the MTS machine to induce a fracture; (d) a failed attempt to create a fracture due to the core crumbling.

Moreover, we executed a wettability experiment utilizing a drop shape analyzer (DSA) on a FORGE core sample (A4-9H, illustrated in **Fig. 7**), yielding compelling outcomes. The experiment unveiled a water-wet behavior, suggesting the core's ability to absorb injected water. This observation indicates that when water interfaces with the surfaces of recently created, reopened, or pre-existing fractures during the advancement of the injected front, it can penetrate the compact matrix as an immobile phase, leading to reduced velocities and fluid entrapment. This discovery offers valuable insights into the matrix's capacity to accommodate water, elucidating its water-holding potential.

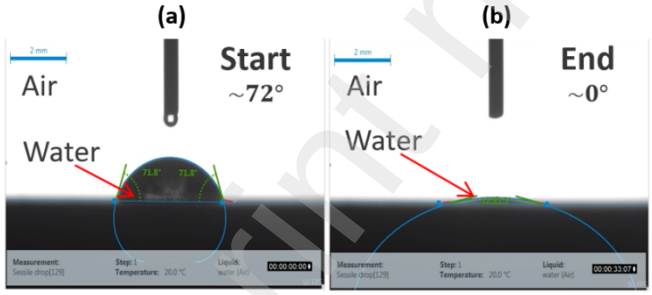


**Fig. 7.** Measurement of contact angle for the granitoid core A4-9H from FORGE: (a) initiation of the experiment with an initial contact angle of 71.8 degrees; (b) conclusion of the experiment at approximately 33 minutes, as the contact angle approached nearly 0 degrees.

## *2.2 Experimental Results*

We initiated laboratory core measurements utilizing an automated core measurement apparatus, both pre- and post-fracture, for two outcrop granite cores—GC1 and GC2 (**Fig. 3-4**, **Table A1**)—and the FORGE horizontal granitoid core, A4-9H (**Fig. 5b**, **Table A2**). However, for the FORGE vertical granitoid core, A3-V (**Fig. 6b**, **Table A3**), we only conducted pre-fracture experiments due to the sample crumbling during the process. The results from these experimental runs are presented in Appendix A (**Tables A1-A3**). Below, we present a schematic of a core sample after fracturing, where **Fig. 8a** provides a more realistic representation, and **Fig. 8b** offers an idealized version of the fractured core assuming uniformity and smoothness of the fracture. Consequently, in **Fig. 8c**, we demonstrate how this assumption simplifies the calculation of fracture aperture (width) by expressing the total surface area of the top of the fractured core in terms of the surface area of the rock matrix ($A_m$) and the surface area of the fracture ($A_f$) (see **Eq. 1 – 6).**

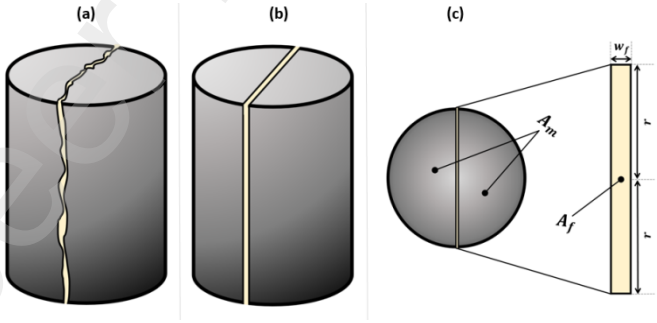


**Fig. 8.** (a) Schematic presenting the layout of the fractured core used in the apparatus measurements; (b) Simplified illustration showcasing the idealized structure of the fractured core; and (c) Top-down view of the idealized diagram illustrating the surface areas of the matrix and fracture, incorporating the aperture.

$$A_t = A_m + A_f = \pi r^2 = \frac{\pi d^2}{4} \quad (1)$$

$$A_f = 2rw_f = dw_f \quad (2)$$

$$\phi_f = \frac{A_f}{A_t} = \frac{2rw_f}{\pi r^2} = \frac{dw_f}{\frac{\pi d^2}{4}} = \frac{4}{\pi d} w_f \quad (3)$$

$$k_f = 10^{\frac{3w_f^2}{12}} \quad (4)$$

$$k_{f,eff} = k_f \phi_f + k_m = \left(\frac{10^3}{3\pi d}\right) w_f^3 + k_m \quad (5)$$

$$w_f = \sqrt[3]{0.003\pi d(k_{f,eff} - k_m)} \quad (6)$$

The tabulated experimental data (**Tables A1-A3**) vividly demonstrate a substantial disparity in core permeability before and after the fracture occurrence. Consequently, within a geological formation, the presence of an accessible conductive fracture, reopening of a sealed fracture, or creation of a new

fracture interconnected with a hydraulic fracture can significantly enhance fluid flow capability within the fracture. Additionally, this augmentation results in a greater rock surface area available for potential circulating fluid in a geothermal system to extract or transport thermal energy. An essential physical characteristic of fractured rock is its effective permeability $(k_{f,eff} = k_f\phi_f + k_m)$, typically significantly higher than the permeability of the surrounding matrix. Therefore, this facilitates the smooth flow of fluids such as water through the fracture when pressure or gravity gradient is exerted on the fluid.

Furthermore, our samples demonstrate significantly low porosity, as indicated in **Tables A1-A3**, even after the fracturing process. A reservoir with exceedingly low porosity suggests that the rock within it has limited capacity to hold fluids like water. Porosity, which measures the volume of void spaces or pores within a rock formation, is a crucial factor in determining the potential fluid storage capacity of a reservoir. In the case of developing a geothermal reservoir with low porosity, specific drilling and completion methodologies may be necessary to enhance connectivity between the wellbore and the accessible pore volume at the rock fracture interface.

Granitoids formed at substantial depths in the Earth's crust experience high temperatures and pressures, resulting in mineral compaction and reduced pore space, ultimately decreasing permeability. The gradual cooling process of deep granitoids, characterized by slow cooling rates, further contributes to their diminished porosity and permeability. During the cooling of magma, minerals undergo extended crystallization, occupying the available pore space. Tectonic stresses prevalent at substantial depths cause mineral compaction, exacerbating the limitation on pore space for fluid flow. Over time, chemical alterations in granitoids, such as hydrothermal modification of minerals like feldspar, lead to increased compactness and reduced pore space (Brown, 2013; Frost et al., 2001). Deep granitoids, due to a confluence of formation-related, cooling, and subsequent geological processes, exhibit extremely low porosity. While this poses challenges for geothermal energy extraction from these reservoirs, advancements in drilling and stimulation technologies hold promise for unlocking their potential. Enhanced Geothermal Systems (EGS) technologies, including hydraulic fracturing and other stimulation methods, offer pathways to augment reservoir permeability, enhance fluid flow, and consequently optimize thermal energy recovery.

### *2.3 FORGE Well 16A(78)-32 Stimulation*

In this subsection, we provide a detailed description of the pressure falloff data obtained during the comprehensive three-stage stimulation of FORGE injection well 16A(78)-32. Our focus is particularly on the hydraulic fracturing (HF) stages conducted in April 2022. The main goal of this analysis is to extract insights from tests based on a modified version of the traditional diagnostic fracture injection test (DFIT). These tests aim to illuminate the effectiveness of the stimulation process within the drainage volume of well 16A(78)-32.

The initial stage of hydraulic fracturing (HF), highlighted in **Fig. 9**, unfolded within a 200 ft open-hole segment. Precisely, this transpired within a measured depth (MD) range of 10,826 ft to 10,828 ft, corresponding to a true vertical depth (TVD) of 8,512 ft. Slickwater was the fracturing fluid utilized during this phase, reaching a peak rate of approximately 50 bpm. The aggregate slickwater volume pumped throughout Stage 1 of HF operations amounted to 4,327 barrels.

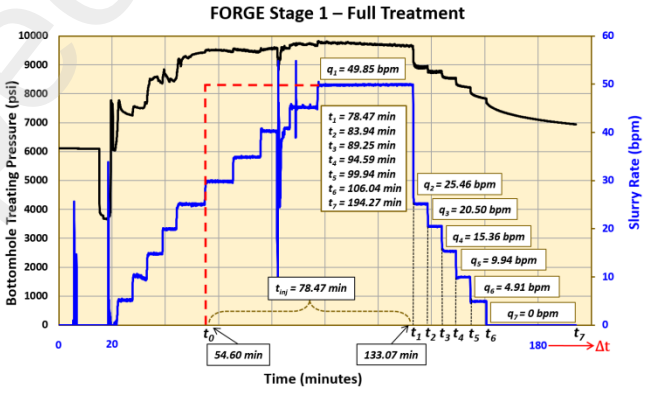


**Fig. 9.** Data from Stage 1 Treatment in FORGE Well 16A(78)-32. The bottomhole treating pressure is indicated in black (psi), while the slickwater rate is illustrated in blue (bpm).

Transitioning to the second phase, illustrated as **Fig. 10,** hydraulic fracturing operations entailed injecting the fracturing fluid into a cased and perforated zone spanning a measured depth (MD) range of 10,560 ft to 10,580 ft, or a true vertical depth (TVD) of 8,471 ft. Much like the prior stage, slickwater served as the fracturing fluid, peaking at a rate of approximately 34 bpm. In this Stage 2 HF, a cumulative volume of 2,777 barrels of slickwater was successfully pumped.

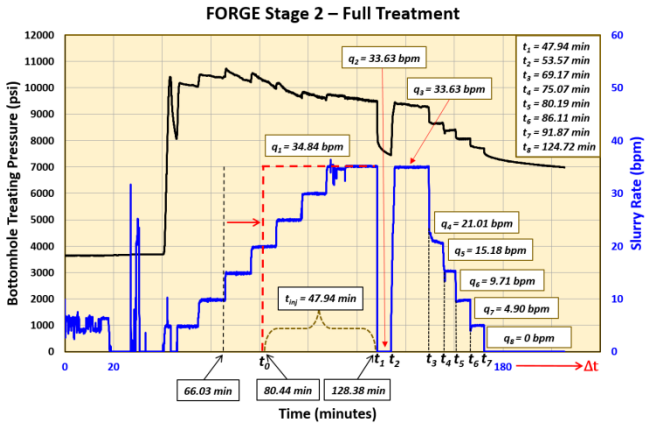


**Fig. 10.** Data from Stage 2 Treatment in FORGE Well 16A(78)-32. The bottomhole treating pressure is indicated in black (psi), while the slickwater rate is illustrated in blue (bpm).

Finally, in the third segment of hydraulic fracturing, indicated as **Fig. 11**, the approach involved injecting the fracturing fluid into a different cased and perforated section spanning from 10,120 ft to 10,140 ft in measured depth (MD), equivalent to 8229 ft in true vertical depth (TVD).

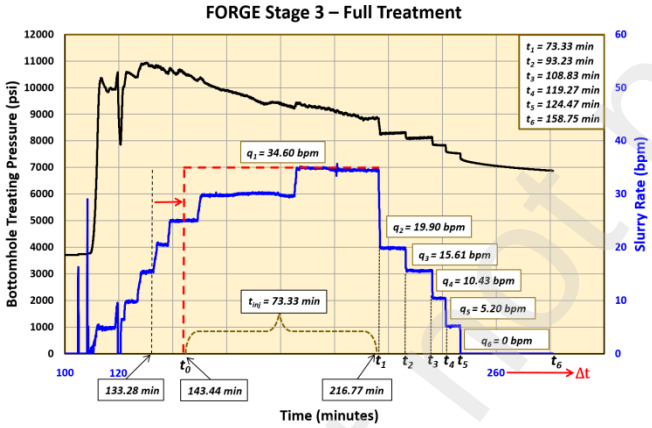


**Fig. 11.** Data from Stage 3 Treatment in FORGE Well 16A(78)-32. The bottomhole treating pressure is indicated in black (psi), while the slickwater rate is illustrated in blue (bpm).

For the third stage, the initiation comprised employing a slickwater pad, succeeded by a crosslinked CMHPG fluid containing DEEPROP™ microproppant. The microproppant possessed mesh sizes of 40/70 (Local/White) and 40/140 (Sand), with concentrations varying from 0.5 to 0.75 pounds of proppant per gallon (PPA). The maximum pumping rate reached approximately 35 bpm during this stage. The cumulative slurry volume pumped throughout Stage 3 HF amounted to 3,016 barrels.

Furthermore, the injected stimulation fluids contained naphthalene sulfonate compounds as tracers (Jones et al., 2023). The tracers were used to determine connectivity and interaction between the three hydraulic fractures. The most significant conclusions from tracer response were that (1) there was little interaction between the three hydraulic stages, and (2) about 2/3 of the tracers were returned, and (3) the returned fluid contained dissolved solids from the formation. While an excellent qualitative analysis of the tracer response was provided by Jones et al. (2023), our future plan is to use a numerical simulator which will include both our pressure transient response results and the tracer data.

### *2.4 Mathematical Background – Pressure Falloff*

The dynamics of water circulation within a fracture network system are intricate, contingent upon various elements encompassing fracture geometry, connectivity, rock hydraulic conductivity, and pressure and temperature gradients within the system. In an EGS, a controlled injection of cold water transpires via an injection well into the subterranean reservoir. As this water navigates through the rock, it encounters fractures and other permeable structures that serve as conduits for its passage. During this journey through fractures, the water interacts with the nearby rock, engaging in thermal and solute exchanges with the rock matrix. Subsequently, the now-heated water, having traversed the reservoir, is extracted via a production well. Understanding the fracture network and its impact on heat extraction can be attained through an analysis of the pressure transient response (B. Mindygaliyeva et al., 2023).

Deciphering the pressure transient behavior of horizontally fractured wells within tight, fractured formations holds significant importance, especially given the intricacy of interpreting pressure transient responses. This complexity stems from the interwoven dynamics involving the horizontal well, hydraulic fracture, natural fractures, and the low-permeability matrix (Medeiros et al., 2007). To comprehend the pressure transient behavior, we effectively employed the methodology outlined below.

The pressure falloff equation for multi-rate in a hydraulic fracture is expressed as:

$$p_i - p_{ws}(t_N + \Delta t) = \underbrace{\frac{4.064\ q_N \mu}{\sqrt{k_{f,eff}}(hL_f)}\left(\frac{1}{(\phi c_t)_{f+m}\mu}\right)^{\frac{1}{2}}}_{slope,\ m} \times \left[\sum_{j=1}^{N} \frac{q_j}{q_N}\left(\sqrt{(t_N + \Delta t) - t_{j-1}} - \sqrt{(t_N + \Delta t) - t_j}\right)\right] \quad (7)$$

Rearranging **Eq. 7**, the pressure at the wellbore at $t_N + \Delta t$ is given by:

$$p_{ws}(t_N + \Delta t) = p_i - \frac{4.064\ q_N \mu}{\sqrt{k_{f,eff}}(hL_f)}\left(\frac{1}{(\phi c_t)_{f+m}\mu}\right)^{\frac{1}{2}} \times \left[\sum_{j=1}^{N} \frac{q_j}{q_N}\left(\sqrt{(t_N + \Delta t) - t_{j-1}} - \sqrt{(t_N + \Delta t) - t_j}\right)\right] \quad (8)$$

The coefficient in front of the bracketed term in **Eq. 8** is given by the absolute value of the slope of the straight-line segment as shown by:

$$m = \frac{4.064 q_N \mu}{\sqrt{k_{f,eff}}\,(hL_f)}\left(\frac{1}{(\phi c_t)_{f+m}\mu}\right)^{\frac{1}{2}} \quad (9)$$

The effective formation permeability of the fracture system is obtained by rearranging **Eq. 9** and is given by:

$$k_{f,eff} = \left(\frac{4.064 q_N \mu}{m(hL_f)}\right)^2 \left(\frac{1}{(\phi c_t)_{f+m}\mu}\right) \quad (10)$$

We opted to concentrate on the experimental outcomes for FORGE Core A4-9H (**Fig. 5b**) under a net confining pressure of 2755 psi (refer to **Table A2**) to derive the fracture aperture ($w_f$) experimentally induced within the core, employing **Eq. 6**. The computed fracture width amounted to 108 $\mu$m. Afterwards, we reevaluated the effective formation permeability ($k_{f,eff}$) utilizing the slope acquired from the analytical analysis of the field data across varying matrix block dimensions ($L_x = L_y$), incorporating the fracture width ($w_f = 108$ $\mu$m) and fracture porosity which was determined by using **Eq. 11**.

$$\phi_f = \frac{w_f(L_x + L_y)}{L_x L_y} \quad (11)$$

*2.5 Analytical Analysis of FORGE Pressure Falloff*

Our analytical approach is firmly grounded in the traditional pressure transient analysis (PTA) widely utilized in petroleum reservoirs. We implemented the superposition principle, specifically utilizing a single-rate solution for linear flow conditions, to scrutinize our multi-rate data. As a result of this analysis, we discerned that the effective permeability within the stimulated volume surpassed the permeability of the reservoir matrix observed in core samples by two orders of magnitude. In the fractured cores, the measured permeability is a blend of the effective permeability of the fracture itself and the permeability of the surrounding matrix. This understanding was then extrapolated to the stimulated volume of Stages 1, 2, and 3 HF in well 16A(78)-32 through numerical modeling and history matching techniques (Kurtoglu et al., 2012).

**Fig. 9-11** showcase the field data for pressure and flow rate during the hydraulic fracturing (HF) treatments for Stages 1, 2, and 3, respectively. The determination of bottomhole treating pressure, measured in psi, involved adding the hydrostatic head of the treating fluid to the surface pressure, excluding friction losses. This approach accounts for the fact that the injected fluid, primarily slickwater with friction-reducing properties, mitigates frictional effects within the wellbore. Moreover, during the pressure falloff period, the injection rate drops to zero, further eliminating friction losses. The resulting calculated bottomhole pressure data is depicted in red, while the slickwater rate in bpm is represented in blue.

By applying the methodology detailed in **Eq. 7 -10**, we conducted a thorough analysis of the pressure falloff behavior in FORGE. The aim was to discern the flow characteristics of both the geothermal reservoir and the well, with a particular emphasis on establishing the effective formation permeability ($k_{f,eff}$). Additionally, we aimed to establish the correlation between this permeability and the presence of stimulated micro- and macro-fractures within the stimulated volume. To pinpoint the straight-line segment within the field data of all of three HF Stages, we graphed $p_{ws}(t_N + \Delta t)$ vs. $\sum_{j=1}^{N} \frac{q_j}{q_N}\left(\sqrt{(t_N + \Delta t) - t_{j-1}} - \sqrt{(t_N + \Delta t) - t_j}\right)$, as depicted in **Fig. 12**. The absolute values of the slopes ($m$) for these segments were calculated to be 278.95, 306.51, and 296.67 for Stages 1, 2, and 3, respectively (**Fig. 12**). The mathematical significance of the slope is defined by **Eq. 10**. Subsequently, we leveraged the slopes derived from the analytical analysis of the field data for the three HF Stages to calculate the effective formation permeability ($k_{f,eff}$), as indicated in **Fig. 12**, employing **Eq. 10** with the following parameters: $h = 2$ $L_f = 656$ ft =200 (Nadimi et al., 2020), $\mu = 0.152$ cP, and $c_t = 6\times10^{-6}$ psi$^{-1}$. This computation was performed for two distinct cases of matrix block dimensions: one with $L_x = L_y = 5$ ft and another with $L_x = L_y = 1$ ft, while maintaining $L_z = 20$ ft. The calculation involved

incorporating the fracture width ($w_f = 108\ \mu m$) and fracture porosity ($\phi f$), determined by **Eq. 11.**

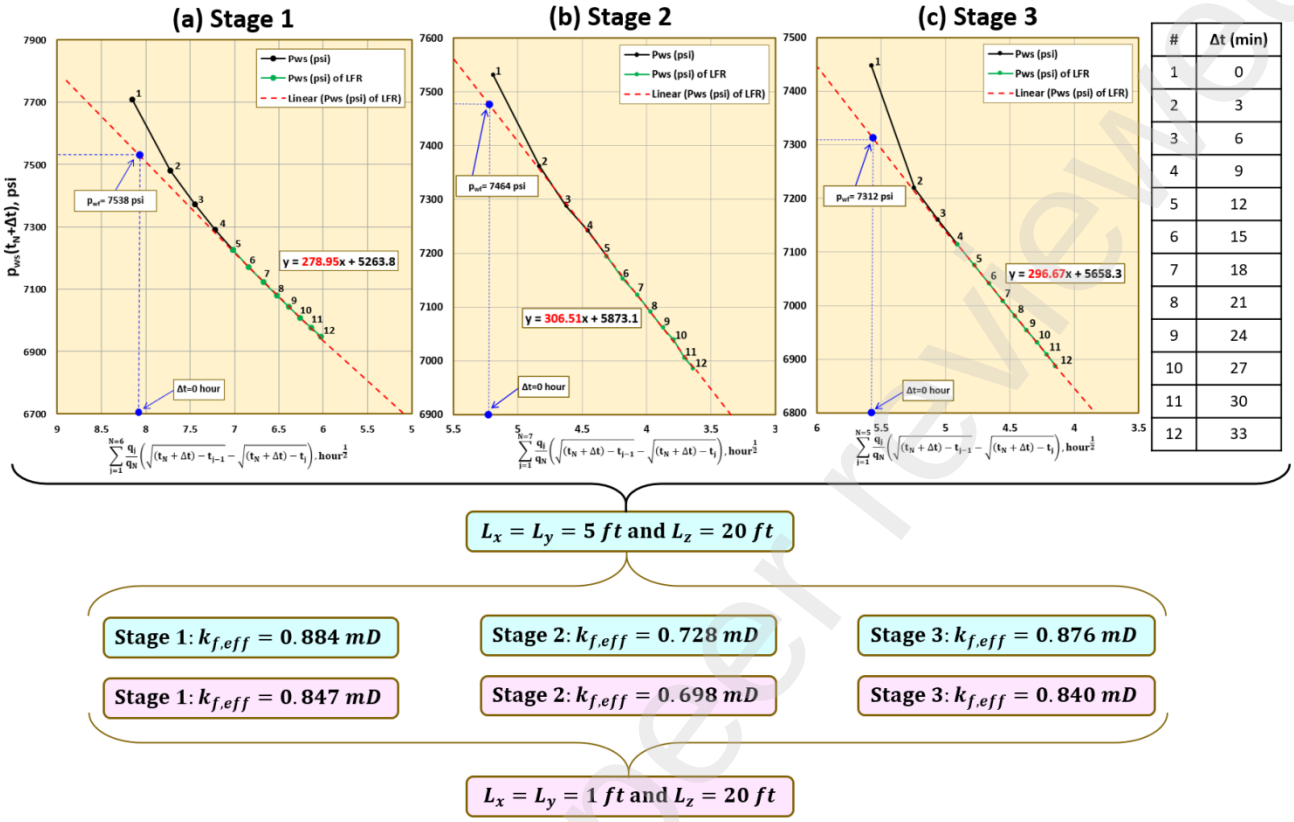


**Fig. 12.** Plot illustrating shut-in bottomhole field pressure data (y-axis) plotted against the summation of time (x-axis). The analytical pressure transient analysis (PTA) results, showcasing effective formation permeability ($k_{f,eff}$), for matrix match-stick block sizes of 5×5×20 ft and 1×1×20 ft, are provided below the plots: (a) Stage 1 involved pumping into a 200 ft long open-hole section (10,826-10,828 ft MD) of the well using slickwater; (b) Stage 2 involved pumping into a cased and perforated zone (10,560 – 10,580 ft MD) of the well using slickwater; (c) Stage 3 involved pumping into a cased and perforated zone (10,120 – 10,140 ft MD) of the well using a slickwater pad initially, followed by a crosslinked CMHPG fluid with DEEPROP™ microproppant (mesh sizes of 40/70 Local/White and 40/140 Sand) at planned concentrations of 0.5 to 0.75 PPA.

### *2.6 Numerical Modeling & Analysis of Pressure Falloff Data*

Subsequent to the analytical analysis of the pressure falloff data, a one-dimensional (1D), dual-porosity model (Alruwayi et al., 2021; Eker et al., 2017) was created to incorporate the impacts of fluid leakage from macro-fractures to the formation matrix rock. This involved considering two distinct matrix block configurations ($L_x = L_y = 5$ ft and $L_x = L_y = 1$ ft, while maintaining $L_z =$ 20 ft). The model was tailored to align with both well pressure data and lab experimental results, particularly utilizing data from FORGE horizontal core A4-9H (**Table A2**) under a net confining pressure of 2755 psi and a pore pressure of 245 psi. The software code used for this model is an internal document. The slopes and effective formation permeabilities ($k_{f,eff}$) obtained from the numerical analysis (refer to **Fig. 13**) strongly coincide with the results derived from the analytical analysis of the FORGE field pressure falloff data. This alignment between the outcomes of these independent mathematical methodologies lends credibility to the potential validity of our analysis.

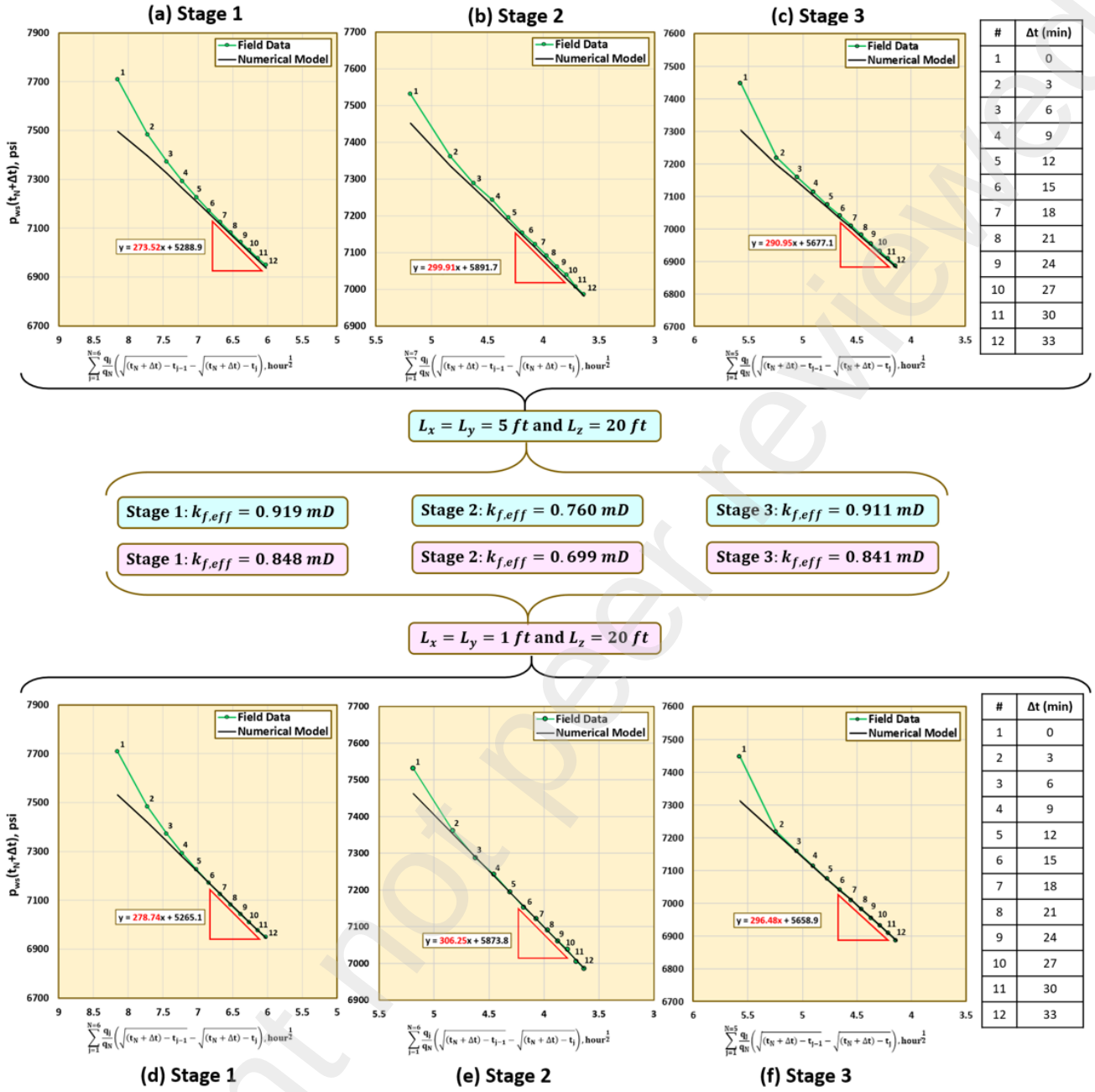


**Fig. 13.** Graph depicting numerical simulation of pressure falloff (in black) and field pressure falloff (in green) on the y-axis against the time summation on the x-axis. The plots showcase results from numerical pressure transient analysis (PTA), specifically revealing the effective formation permeability ($k_{f,eff}$). The analysis utilized a 1D dual-porosity numerical model considering matrix match-stick block sizes of 5×5×20 ft (Sections: a-c) and 1×1×20 ft (Sections: d-f), incorporating the $k_{f,eff}$ obtained from analytical PTA as an input variable.

The permeability of fractures, determined via pressure falloff analysis and numerical modeling, is noticeably influenced by the dimensions of the matrix blocks. We regard these dimensions as a statistical representation of fracture spacings within conductive fractures. Utilizing the effective formation permeability derived from FORGE field data and assuming a matrix block size of 5 ft, we computed an intrinsic permeability for the fractures of 12,500 mD. In a similar vein, assuming a matrix block size of 1 ft, we established an intrinsic permeability for the fractures of 2,400 mD. Thus, presuming that a fracture spacing of 5 ft is more representative of the stimulated FORGE environment, we can deduce that the intrinsic permeability of the

macro-fractures falls within the range of approximately 12,500 to 13,000 mD.

Another notable source of uncertainty in determining the permeability of the stimulated formation is the hydraulic fracture height, which we assumed to be 656 ft. If we consider a fracture height of 328 ft, the calculated effective fracture permeability would increase fourfold (specifically, from 0.884 mD to 3.534 MD). This uncertainty can be reduced significantly if accurate measurements of both the length and height of the hydraulic fracture are obtained through suitable field methods, such as microseismic techniques.

### *2.7. Ongoing Modeling Efforts*

Besides numerical modeling of the pressure falloff data of FORGE's injection well, we constructed two additional distinct numerical models (1) to quantify the injected fluid loss volume to the formation pores and macro-fractures and (2) to determine the temporal evolution of temperature distribution in the entire circulation flow path.

#### *2.7.1 Injected Water Loss Model*

The grid system used for evaluating the injected water loss from each hydraulic fracture stage to the surrounding hot dry rocks is presented in **Fig. 14**. The model input data includes matrix permeability and porosity derived from core analysis. The system is a highly fine-grid near the walls of the hydraulic fractures. The effective formation permeability near hydraulic fracture walls has values obtained from the falloff analysis and decreases logarithmically away from the walls.

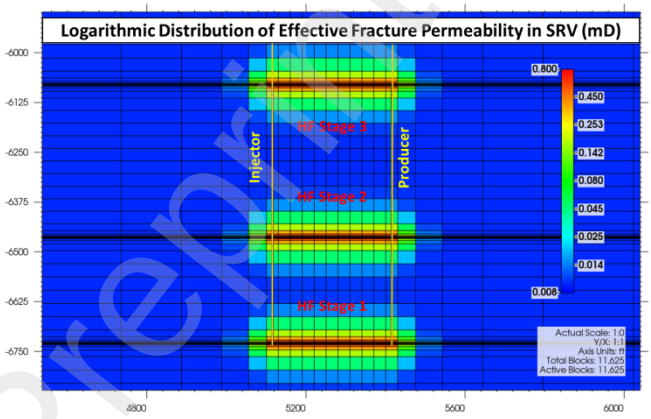


**Fig. 14.** The grid system and effective formation permeability used in evaluating the injected water loss from each hydraulic fracture stage to the surrounding hot dry rocks. The grid system is a highly fine grid near the hydraulic fracture walls.

The water saturation distribution after two years of injection-production via the well pair system is presented in **Fig. 15**. The water loss to the formation was about 16 % of the total injected water in two months and 4% in two years.

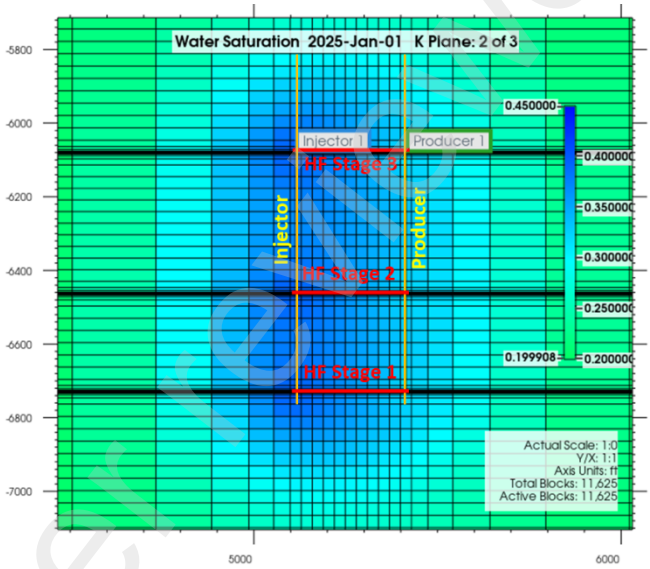


**Fig. 15.** Water saturation distribution in the rock matrix after 2 years of water injection.

#### *2.7.2 Heat Extraction Model*

The heat transfer equations in the x-y-z domain (x the horizontal coordinate parallel to the fracture face, y the horizontal coordinate perpendicular to fracture face, and z the vertical coordinate parallel to the fracture face) are:

1. Heat flow balance within each hydraulic fracture consists of advection of heat along the fracture aperture and heat conduction at the fracture-formation rock walls:

$$\underbrace{-\left(\rho_w c_w u_{x,w,hf}\frac{\partial T_{w,hf}}{\partial x}\right)}_{Heat\ Advection\ in\ HF} \underbrace{-\left[-\left(\frac{K_{R,y}}{w_{hf}/2}\right)\frac{\partial T_R}{\partial y}\Big|_{y=w_{hf}/2}\right]}_{Conduction\ of\ Heat\ at\ the\ Fracture-Matrix\ Interface} = \underbrace{\rho_w c_w \frac{\partial T_{w,hf}}{\partial t}}_{\substack{Rate\ of\ Heat\ Accumulatio\ in\ the\ Fracture}} \quad (12)$$

2. Heat flow balance in the rock surrounding hydraulic fracture, dominated by heat conduction:

$$\underbrace{\frac{\partial}{\partial x}K_{R,x}\frac{\partial T_R}{\partial x}+\frac{\partial}{\partial y}K_{R,y}\frac{\partial T_R}{\partial y}+\frac{\partial}{\partial z}K_{R,z}\frac{\partial T_R}{\partial z}}_{\substack{Heat\ conduction\\ in\ the\ rock\ matrix\\ surrounding\ fracture}}=$$

$$\underbrace{\rho_R c_R\frac{\partial T_R}{\partial t}}_{\substack{Rate\ of\ heat\\ accumulation\\ in\ the\ rock\ matrix}} \tag{13}$$

From mathematical perspective and for simplicity we assume no heat flow in the rock halfway between two hydraulic fractures which we present it mathematically by the following equation:

$$\left.\frac{\partial T_R}{\partial y}\right|_{y=\mathrm{L}_y/2}=0 \tag{14}$$

At every hydraulic fracture inlet, the flow velocity is assumed equal to the injection rate divided by the fracture aperture cross-sectional area. This is influx boundary condition at each fracture entrance that is mathematically stated by the following equation:

$$u_{x,w,hf}|_{x=0}=q_{inj}/(w_{hf}h) \tag{15}$$

The solution method for the above set of equations is a time implicit, finite-difference procedure in the 3D space which is presented in Appendix B. The computation grid used in obtaining the solution is shown in Figure 16. An example solution of temperature distribution in formation for an ideal FORGE well doublet conditions is presented in **Fig. 17**.

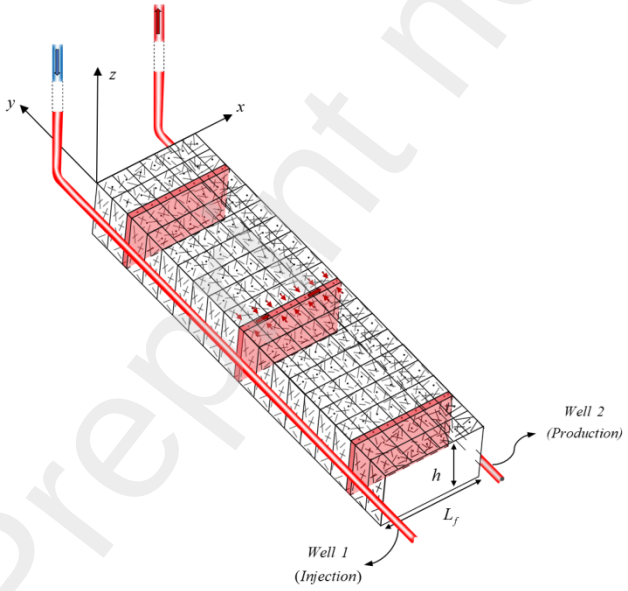


**Fig. 16.** Grid system used in the numerical solution of Utah FORGE injection-production well heat extraction model.

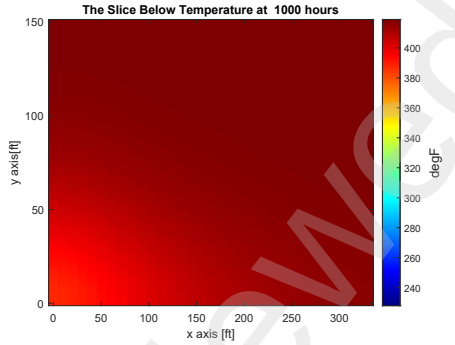


(a) The layer above the HF drainage volume

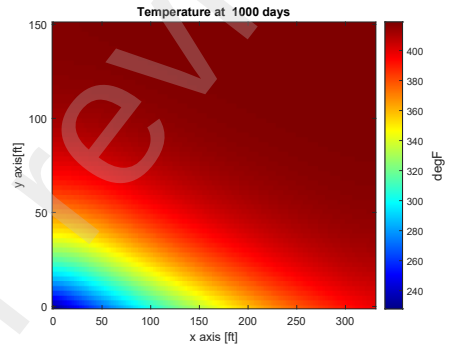


(b) The HF main drainage volume

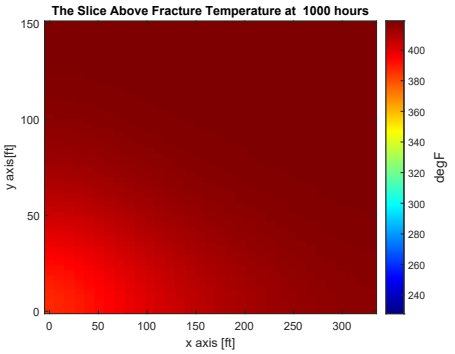


(c) The layer below the HF drainage volume

**Fig. 17.** (a) Temperature distribution in the layer above the hydraulic drainage volume. (b) Temperature distribution within the heat drainage volume (i.e., the middle layer of the model) in the half-space of a single hydraulic fracture after 1000 days when injection rate into this fracture is 1200 barrels of water per day. The surface injection temperature is 200 °F and the bottom hole temperature at the fracture-production well is 397 °F. (c) Temperature distribution in the layer below the hydraulic drainage volume.

The heat extraction includes both heat balance between flowing water in the hydraulic fractures and the formation (**Fig. 17**) and heat transfer in the injection-production well columns (**Fig. 18**). In the injection well, the injected cool water gradually collects heat from the wellbore surrounding as it moves downward in the well before entering hydraulic fractures. The amount of warming is a function of

injection rate and the well configuration. Once the water enters the hydraulic fracture, it further collects heat as a function of the advective flow velocity within the fracture. For optimal heat gathering efficiency, we need to maintain a water advective velocity in the fracture that is approximately equal or somewhat smaller than the fracture length per day. Once the heated water exits the fracture and enters the production well it will begin to lose some amount of heat to the wellbore surrounding formation through the casing and cement sheath inside the production well (Augustine, 2016; Gringarten et al., 1975). The equation we use calculate the heat transfer in the injection and production wells has the following form:

$$-\rho_w C_w(u_{w,z})\frac{\partial T}{\partial z} + \left[\frac{1}{r}\frac{\partial}{\partial r}\left(rK\frac{\partial T}{\partial r}\right)\right]_{r_1} = \rho_w C_w \frac{\partial T}{\partial t} \quad (16)$$

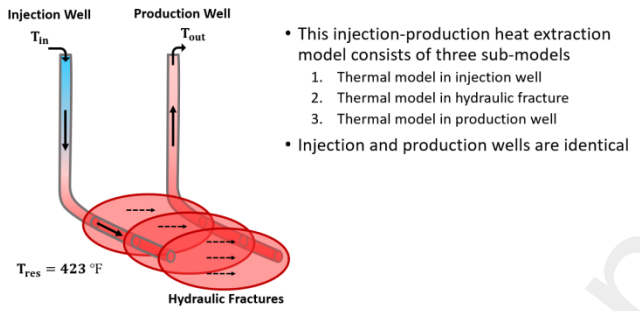


**Fig. 18.** Heat Extraction Model: Schematic representation of the FORGE injection-production system showcasing the heat extraction process.

### *2.8 Relevant Economics*

The most important factor in the EGS economics is the power generation capacity of the system, which is driven by the deliverability of the induced fractures; that is, the total heat exchange drainage volume (HEDV) and the advective flow velocity of circulating water. The second factor is the decline rate of the fracture system power generation capacity over time. The power generation decline rate is controlled by the uniformity of the flow conformance of the circulating injection water in the fracture system, i.e., minimizing water short-circuiting that causes premature cooling of the circulating water. (Fleckenstein et al., 2023b)

## 3 Overview of Fervo Energy's EGS Pilot Test in Northern Nevada

**Fervo Energy**, an EGS company, has vigorously pursued development of a nearfield, commercial enhanced geothermal system project adjacent to the Blue Mountain hydrothermal field in Nevada, aiming to boost electricity generation at the existing **Blue Mountain power facility**. Fervo also has broken ground on a new EGS project for its greenfield development plan in Southwest Utah, adjacent to the DOE's FORGE project.

**Fervo Energy,** in its EGS pilot test (Project Red) initiated in 2022 and completed testing in 2023, demonstrated the technical ability to complete two successful horizontal geothermal wells (a 'doublet') with 3,000+ feet of lateral length in each well, as part of a long-term strategic reservoir management protocol which aligns closely with FORGE's mission of advancing EGS development and commercialization (Norbeck and Latimer, 2023).

The **injection well** was designated (34A-22), **production well** (34-22), and the **observation well** (73-22), a purely vertical well is located roughly 700 feet to the north of the injection well's horizontal lateral midpoint section (Norbeck et al., 2023), with the producer positioned 400 feet horizontally to the north of the injector (Titov et al., 2023), refer to **Fig. 19 and Table 1).**

**Table 1.** Well data for the three wells depicted in **Fig. 19** of the Blue Mountain Enhanced Geothermal System (EGS) pilot test (Fercho et al., 2023; Norbeck and Latimer, 2023; Titov et al., 2023).

| Parameter | Monitoring Well | Injector Well | Producer Well |
|---|---|---|---|
| Well Name | 73-22 | 34A-22 | 34-22 |
| Measured Depth, MD (ft) | 8009 | 11220 | 11225 |
| True Vertical Depth, TVD (ft) | 7998 | 7664 | 7524 |
| Lateral Length (ft) | – | 3521 | 3310 |
| Drilling Time (day) | 41 | 72 | 59 |
| Number of Stages | – | 16 | 20 |
| $q$ Range (gpm) | – | 650-850 | 550-750 |
| $q_{max}$ (gpm) | – | 1003 | 970 |

The doublet wells drilled diameters were 9 7/8 inches and were completed with a 7-inch casing. The measured formation temperature at the horizontal sections was 376 °F. The fracturing treatment design for injection well (34A-22) included 16 hydraulic fracture stages, each stage consisting of six clusters of perforations and six perforations per cluster in a 150-foot section, except for stages 12 and 13 which had 9 clusters per stage and varying perforations. The hydraulic fractures were placed using the plug and perf method. The treatment design consisted of injecting 16,000 barrels of stimulation fluid at a target rate of 100 barrels per minute and 540,000 pounds of proppant per

hydraulic fracture stage. The injected stimulation fluid was slickwater with a low concentration of friction reducers. The proppant was a mixture of 40/70 and 100 mesh silica sand at 0.25 to 1.5 pounds per gallon concentrations. The hydraulic fractures emanated in the injection well (34A-22) communicated effectively with the producer well (34-22) with an average offset spacing between injector and producer of 365 feet (Norbeck and Latimer, 2023).

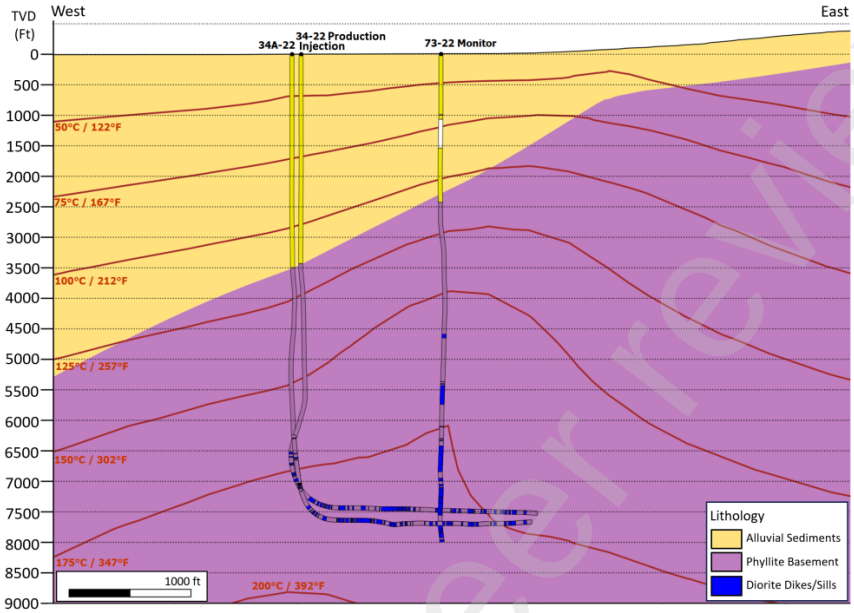


**Fig. 19**. The Horizontal Doublet in Blue Mountain Enhanced Geothermal System with the Adjacent Deep Vertical Monitoring Well (Norbeck and Latimer, 2023).

Figure 20, as documented by Norbeck and Latimer (2023), displays the recorded flow rates and wellhead pressures from the 37-day circulation test conducted in Injection Well 34A-22 (top) and Production Well 34-22 (bottom).

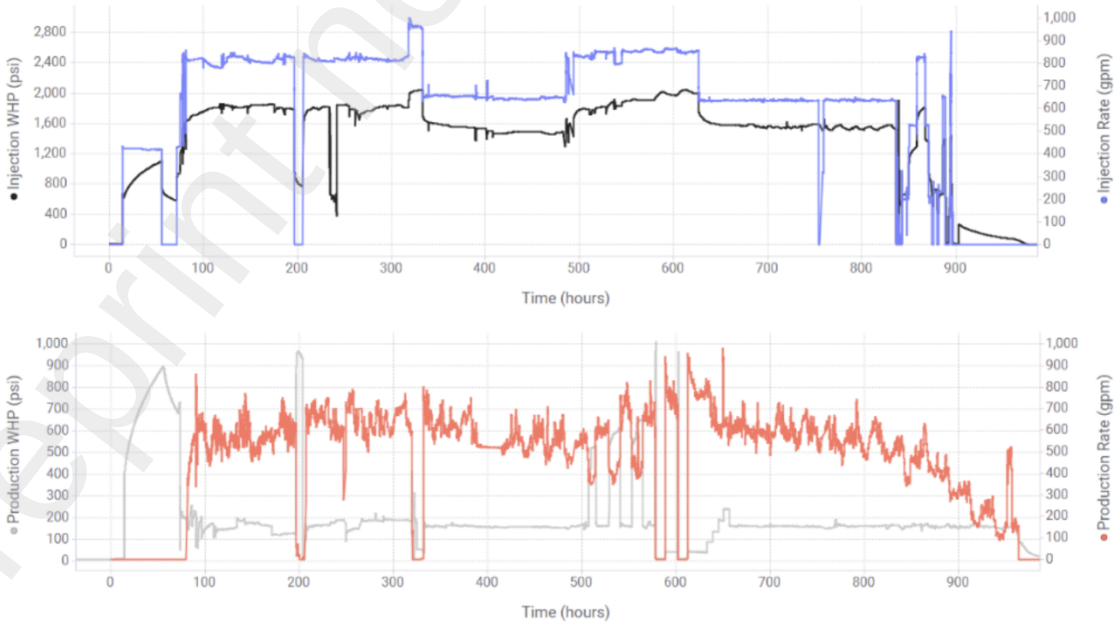


**Figure 20**. Recorded flow rate and wellhead pressure during the 37-day circulation test in Injection Well 34A-22 (top) and Production Well 34-22 (bottom) (Norbeck and Latimer, 2023).

The pilot test included a cross flow test and the use of a **wireline injection logging** (**Fig. 21**) to determine the distribution of the injected water into individual fracture clusters in the injection well. Results reveal the degree of non-uniformity of water entering each hydraulic fracture stage. Throughout the crossflow test, the production fluid temperature displayed a continuous increase, suggesting the absence of severe thermal short-circuit pathways generated during the stimulation treatment.

During the entire crossflow test, the injection rates within the system were solely driven by surface injection pumps which affirmed that the Enhanced Geothermal System (EGS) pilot test behaved as a relatively excellent confined system with no indication of the need for artificial lift to sustain flow rates in the production well.

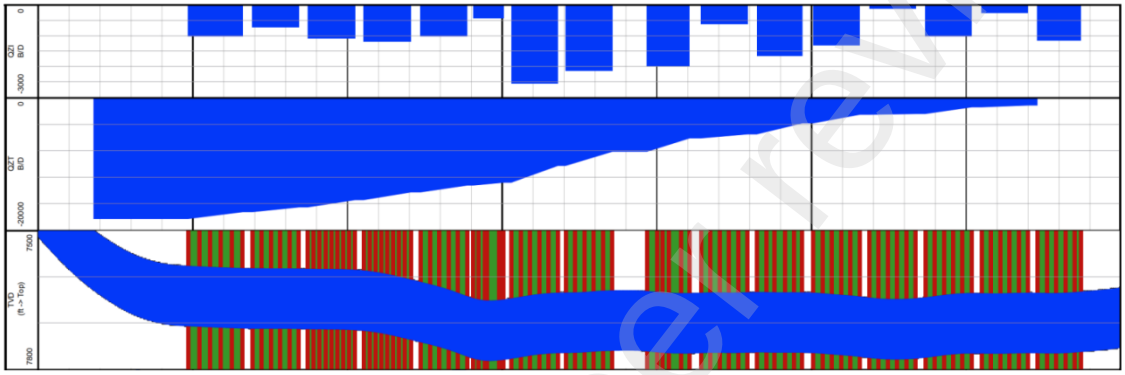

**Fig. 21**. Spinner log survey conducted in Injection Well 34A-22 during the crossflow test. The flow profile graph provides the injection rate distribution into individual stages along the lateral (top), the cumulative injection rate profile along the lateral (middle), and the number and location of perforation clusters along the lateral (bottom). The spinner log injection rate profile was obtained using a constant injection rate of 12.5 bpm (Norbeck and Latimer, 2023).

Comparisons of the peak injection rates observed in extended flow rate tests following stimulation in several prominent EGS projects worldwide can be seen in **Fig. 22**. The figure, from paper by Norbeck and Latimer (2023), includes peak injection rates observed in Fervo's Injection Well 34A-22 and Production Well 34-22 during the 37-day crossflow test.

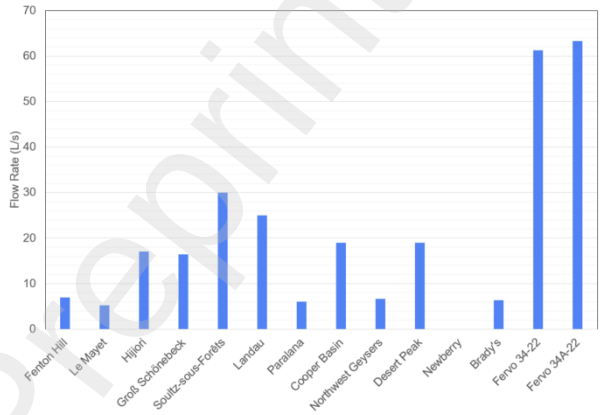


**Fig. 22**. Comparison of Peak Injection Rates Observed in Extended Flow Rate Tests Following Stimulation Phases in Various Prominent EGS Projects Worldwide (Norbeck and Latimer, 2023).

The well performance results underscore that the implementation of the two-horizontal well design, combined with multistage stimulation treatments involving proppant, has yielded the most productive EGS system reported thus far in the World.

### *3.1 Analysis of Two Different Pressure Falloff Tests in the Fervo Energy's Project*

Initially, a continuous-rate injection period at around 10 bpm was maintained for approximately 43 hours, during which the production well was temporarily shut-in resulting in a 12-hour pressure falloff period. Subsequently, an estimated *net average* constant-rate injection of about 6 bpm, factoring in production activity, for a duration of approximately 113 hours, followed by a shorter 7-hour falloff period.

Our approach, detailed in **Eq. 7** – **10**, mirrors the methodology employed in our FORGE pressure transient analysis. The slopes obtained from the straight-line segments of the first and second pressure falloffs were 73.28 psi/hr$^{1/2}$ and 62.44 psi/hr$^{1/2}$, respectively (refer to Appendix C). The following input

parameters were utilized in analysis of pressure falloffs in Fervo Energy's Blue Mountain EGS project via **Eq.10**:

$h = 300\ ft$
$L_f = 365\ ft$
$\mu = 0.3\ cP$
$c_t = 6 \times 10^{-6}\ psi^{-1}$
$\phi_m = 0.0065$
$\phi_f = 2.92 \times 10^{-4}$ (Applied Eq. 11)
$L_x = L_y = L_z = 5$ ft
$n_{hf} = 50$
$w_{hf} = 223\ \mu m$ (when $n_{hf} = 50$, see Appendix D)

When determining the effective formation permeability ($k_{f,eff}$), we employed a coefficient of 4.064 in **Eq. 10** for the initial falloff and a coefficient of 8.128 for the subsequent falloff in **Eq. 10**. The first test involved shutting down production, aligning with our assumption of a two-sided fracture (two wings), justifying the use of a coefficient of 4.064. In contrast, during the second test, both the injector and producer were active before shutting down the injector. In this scenario, it is reasonable to assume a one-sided fracture (dominated by one wing connected to the producer), leading to the use of a coefficient of 8.128. Despite efforts, it is challenging to account for all idiosyncrasies and variations in pressure falloffs. As a result, our findings yielded effective permeabilities of 0.6 mD for the first pressure falloff and 0.3 mD for the second pressure falloff.

## 4 Discussion

Laboratory assessments of the cores encompassed unfractured and fractured samples from both outcrop granite and FORGE granitoid. In all cases, these cores displayed very low matrix permeabilities and porosities (~0.001 mD and ~0.5%, respectively). These variations in properties can be attributed to the differing geological conditions of their formation. The outcrop granite core, being from a surface location, underwent atmospheric weathering. Conversely, the granitoid cores, sourced from deep within the Earth, endured high levels of stress and temperature.

In comparing the matrix permeability of the granitoid cores to the effective formation permeability determined through pressure falloff analysis (PTA), significant disparities were evident. The PTA outcomes revealed effective formation permeabilities that were two to three orders of magnitude greater than the matrix permeabilities of the granitoid cores. This points to the likely existence of permeable macro-fractures and micro-fractures, which could result from fracture generation or the reactivation of existing fractures. The methodology employed mirrored that utilized for unconventional reservoirs to ascertain the degree of short-circuiting of the injected fluid in the FORGE hot, dry rock.

Furthermore, a wettability experiment conducted on a FORGE core (A4-9H) unveiled a water-wet behavior, underscoring its capacity to absorb injected water. This implies that water might infiltrate the tight matrix as an immobile phase, providing insights into the potential water retention capacity of the matrix.

Overall, the laboratory core assessments furnished valuable insights into the porosity, permeability, and wettability of the examined cores, illuminating the presence of fractures and their influence on fluid movement within the rock formations.

In addition to our focused analysis of the Utah FORGE project, we also have carefully examined the flow test data from the Blue Mountain EGS commercial site in Nevada, as well as the analysis conducted by Norbeck and Latimer (2023). We believe Norbeck and Latimer have provided a credible engineering analysis for the Blue Mountain EGS pilot test data; however, we have included additional perspectives via two pressure falloff analyses and further analysis and interpretation of the calculated fracture conductivity between the injection-production well pairs.

The Blue Mountain EGS test results are consistent with our FORGE findings the formation system is (1) hot dry rock, (2) formation permeability and porosity are very small, and (3) the hydraulic fracturing field trials both in Utah FORGE and Blue Mountain EGS pilot site stimulate the formation rock causing creation of micro- and macro-fractures between each stage. In fact, we believe that the Blue Mountain EGS pilot test indicates that the stimulated volumes between different stages have different flow conductivities as evidenced by the injection logging data (Norbeck and Latimer, 2023). Ultimately, the straightforward computation of hydraulic fracture conductivity, based on application of Darcy's Law by Norbeck and Latimer (2023) and the measured pressure differential between injector and producer wells, yields a pragmatic value for the calculated ***hydraulic fracture conductivity*** ($k_{hf}w_{hf}$), which we subsequently employed to calculate an average ***hydraulic fracture width*** ($w_{hf}$) of 223 $\mu m$

using an average of 50 equal-thickness hydraulic fractures ($n_{hf}$) in the pilot test and applying Poiseuille's Law. When we use an average of 100 major hydraulic fractures, the average fracture width decreases to 177 $\mu m$, and if we use an average of 20 major hydraulic fractures, the average fracture width increases to 303 $\mu m$ (see Appendix D).

## 5 Conclusions

Geothermal energy is heat within the Earth. It is an abundant, renewable energy source because heat is continuously produced inside the Earth. There are two types of geothermal reservoirs. The first type, the hydrothermal (HT) reservoirs, are subsurface porous and permeable hot rocks saturated with mobile hot water that can be withdrawn to the surface via production wells for electricity generation without any major reservoir stimulation. The second type consists of hot dry rock (HDR) systems where the rock has very low permeabilities and does not contain water; thus, requiring formation stimulation to generate permeability and injection of water to permeate the rock.

The movement of water within an interlinked fracture system is a complex process influenced by numerous factors. These include the shape and connectivity of fractures, the hydraulic conductivity of the rock, and the pressure and temperature gradients within the system. In Enhanced Geothermal Systems (EGS), the initial step involves injecting cold water into an underground reservoir via an injection well. As this water moves through the rock, it encounters fractures and other permeable structures that act as conduits for its flow. During this passage through the fractures, the water interacts with the surrounding rock, leading to exchanges of heat and solutes with the rock matrix. After circulating through the reservoir, the heated water is extracted through a production well.

The following are our specific accomplishments:

1. We have presented analyses of laboratory and field data indicating that the current two-well, injection-production system, connected with multiple hydraulic fractures, is the most promising method for extracting heat from HDR systems to generate electricity given the abundance of HDR systems in the Earth's crust.
2. The current two-well system could be expanded to a three-well system consisting of one injection well and two symmetric producing wells connected with hydraulic fractures.
3. To improve economics, the use of a newly designed well stimulation technique, the **GeoThermOPTIMAL,** presented elsewhere, is a more cost-effective well stimulation technique than the common plug-and-perf stimulation technique.
4. We conducted analytical and numerical modeling of the pressure falloff data obtained from the three hydraulic fracturing (HF) stages (Stages 1, 2, and 3) in the FORGE injection well 16(A)78-32. Our analyses revealed the presence of highly conductive micro- and macro-fractures in the three FORGE HF Stages.
5. Using cores from an outcrop granite and FORGE granitoid rocks, we determined the permeability and porosity of the matrix rock. Then, we created a single macro-fracture in each core plug to measure the enhanced permeability of the fractured core sample under confining stress. The measurements provided information and shed light on the nature of micro- and macro-fractures under downhole settings in Utah FORGE formation.
6. The properties measured in the laboratory for the outcrop granite and FORGE granitoid rock samples were integrated into the analysis of several shut-in pressure tests. These analyses provided us with insight to develop both quantitative and qualitative measures for the stimulated volume in the FORGE and Blue Mountain EGS projects.
7. The calculated permeability values of fractures in the stimulated volume, determined via FORGE and Blue Mountain EGS pressure falloff analysis, are somewhat affected by the dimensions of the matrix blocks which would serve as a statistical measure of the spacing between conductive fractures. We also concluded that the intrinsic permeabilities of the stimulated fractures range from $10^3$ to $10^4$ mD for FORGE and somewhat larger for Blue Mountain EGS.
8. The application of reservoir engineering methods, akin to the ones used in the pressure falloff analysis of unconventional oil and gas reservoirs and FORGE, along with numerical modeling, offered the essential insights needed for enhancing the efficiency of heat extraction from EGS reservoirs.

**Acknowledgments**

The material presented in this paper consists of two parts: **First**, analysis of data from Utah FORGE field research with funding support by the Department of Energy, Office of Energy Efficiency and Renewable Energy (EERE), under Award Number DE-EE0007080. This report was prepared as an account of work sponsored by an agency of the United States Government. Neither the United States Government nor any agency thereof, nor any of their employees, makes any warranty, express or implied, or assumes any legal liability or responsibility for the accuracy, completeness, or usefulness of any information, apparatus, product, or process disclosed, or represents that its use would not infringe privately owned rights. Reference herein to any specific commercial product, process, or service by trade name, trademark, manufacturer, or otherwise does not necessarily constitute or imply its endorsement, recommendation, or favoring by the United States Government or any agency thereof. The views and opinions of authors expressed herein do not necessarily state or reflect those of the United States Government or any agency thereof.

**Second**, we used publicly available data from Fervo Energy's 2023 field pilot project reported in several papers. We are very grateful to Fervo for this opportunity.

**Third**, we acknowledge the use of Computer Modeling Group Ltd. (CMG) and MATLAB software in addition to our own in-house numerical models.

**Nomenclature**

$\mu =$ Slickwater viscosity, cP

$\phi_{PVC} =$ Polyvinyl chloride (PVC) tape's porosity

$\phi_t =$ Total porosity, fraction

$\phi_f =$ Fracture porosity , fraction

$\phi_m =$ Matrix porosity, fraction

$A =$ Coefficient matrix of heat flow equations

$A_t =$ Top circular surface area of cylinder, $\mu m^2$

$A_f =$ Surface area of fracture in the cyliner top , $\mu m^2$

$A_m =$ Surface area of matrix in the cyliner top, $\mu m^2$

$c_t =$ Total compressibility, $psi^{-1}$

$d =$ Core sample diameter, μm

$h =$ Formation thickness, ft

$j =$ Number of rate steps: 1, 2, ..., N

$k_f =$ Fracture permeability, mD

$k_{f,eff} =$ Effective formation permeability, mD

$k_{f,eff,core} =$ Core's effective formation permeability, mD

$k_m =$ Matrix permeability, mD

$L_x =$ Matrix block side length in the x-direction, ft

$L_y =$ Matrix block side length in the y-direction, ft

$L_z =$ Matrix block side length in the z-direction, ft

$L_f =$ Fracture half-length, ft

$m =$ Slope of the straight-line segment (PTA)

$p_i =$ Initial pressure, psi

$p_{ws} =$ Shut-in bottomhole pressure, psi

$q_j =$ Rate at step number $j$, bpd

$q_N =$ Final rate before shut-in, bpd

$\vec{R} =$ Column vector of residuals in the heat flow equations

$t =$ Time, hr

$t_N =$ Starting time of shut-in period, hr

$t_{inj} =$ Pumping time, min

$T =$ Temperature, °F

$\vec{T} =$ Temperature vector column in heat flow equations, °F

$\Delta t =$ Shut-in time, hr

$w_f =$ Fracture width or aperture, μm

**Declaration of Competing Interest**

The authors declare that they have no known competing financial interests or personal relationships that could have appeared to influence the work reported in this paper.

**References**

Allis, R., Moore, J.N., 2019. Geothermal Characteristics of the Roosevelt Hot Springs System and Adjacent FORGE EGS Site, Milford, Utah. Utah Geological Survey Miscellaneous Publication 169.

Alruwayi, S.A., Uzun, O., Kazemi, H., 2021. Matrix Refinement in Mass Transport Across Fracture-Matrix Interface: Application to Improved Oil Recovery in

Fractured Reservoirs, in: Day 1 Mon, November 15, 2021. SPE. https://doi.org/10.2118/208038-MS

Augustine, C., 2016. A Methodology for Calculating EGS Electricity Generation Potential Based on the Gringarten Model for Heat Extraction From Fractured Rock, NREL. GRC Transactions, Vol. 40.

Brown, M., 2013. Granite: From genesis to emplacement. GSA Bulletin 125, 1079–1113. https://doi.org/10.1130/B30877.1

Casteel, J., Trazona, R., Melosh, G., Niggemann, K., Fairbank, B., 2010. A Preliminary Conceptual Model for the Blue Mountain Geothermal System, Humboldt County, Nevada. Proceedings World Geothermal Congress 2010, Bali, Indonesia, 25-29 April 2010 .

Cho, Y., 2012. Effects of pressure-dependent natural-fracture permeability on shale-gas well production. MS thesis, Colorado School of Mines, Golden, Colorado, USA. http://hdl.handle.net/11124/16314.

DiPippo, R., 2005. Chapter 1 - Geology of Geothermal Regions, in: DiPippo, R. (Ed.), Geothermal Power Plants. Elsevier Science, Oxford, pp. 3–19. https://doi.org/https://doi.org/10.1016/B978-185617474-9/50032-7

Eker, E., Uzun, I., Kazemi, H., 2017. Numerical Simulation of Dual-Porosity Multiphase Flow Using Poroelasticity Theory, in: Day 3 Wed, February 22, 2017. SPE. https://doi.org/10.2118/182728-MS

Fercho, S., Norbeck, J., McConville, E., Hinz, N., Wallis, I., Titov, A., Agarwal, S., Dadi, S., Gradl, C., Baca, H., Eddy, E., Lang, C., Voller, K., Latimer, T., 2023. Geology, State of Stress, and Heat in Place for a Horizontal Well Geothermal Development Project at Blue Mountain, Nevada. SGP-TR-224, Proceedings , 48th Workshop on Geothermal Reservoir Engineering. Stanford University, Stanford, California, February 6-8, 2023.

Fleckenstein, W.W., Kazemi, H., Miskimins, J.L., Eustes, A.W., Abdimaulen, D., Mindygaliyeva, B., Uzun, O., Amini, K., Hill, T., Mailand, J., Henschel, R., King, G., Ortiz, S., Keyes, C., 2023a. Development of Multi-Stage Fracturing System and Wellbore Tractor to Enable Zonal Isolation During Stimulation and Enhanced Geothermal System Operations in Horizontal Wellbores - First Year Progress, in: Day 3 Wed, October 18, 2023. SPE. https://doi.org/10.2118/215107-MS

Fleckenstein, W.W., Kazemi, H., Royer, C., Loff, G., Zimmermann, J., 2023b. A Stochastic Economic Analysis of an Enhanced Geothermal System. Geothermal Rising Conference, October 1-4, 2023, Reno, NV.

Fleckenstein, W.W., Miskimins, J., Kazemi, H., Eustes, A., Abdimaulen, D., Mindygaliyeva, B., Uzun, O., Amini, K., Hill, T., Mailand, J., Henschel, R., King, G., Ortiz, S., Keyes, C., 2022. Development of Multi-Stage Fracturing System and Wellbore Tractor to Enable Zonal Isolation During Stimulation and EGS Operations in Horizontal Wellbores. SPE Annual Technical Conference and Exhibition. https://doi.org/10.2118/210210-MS

Frost, B.R., Barnes, C.G., Collins, W.J., Arculus, R.J., Ellis, D.J., Frost, C.D., 2001. A Geochemical Classification for Granitic Rocks. Journal of Petrology 42, 2033–2048. https://doi.org/10.1093/petrology/42.11.2033

Geology, 2022. Geology | Open Energy Information. Utah FORGE Geology. https://openei.org/wiki/Geology .

Gringarten, A.C., Witherspoon, P.A., Ohnishi, Y., 1975. Theory of Heat Extraction From Fractured Hot Dry Rock. Journal of Geophysical Research (1896-1977) 80, 1120–1124. https://doi.org/https://doi.org/10.1029/JB080i008p01120

Hill, L.B., 2021. Superhot Rock Geothermal: A Vision for Zero-Carbon Energy “Everywhere”. https://www.catf.us/wp-content/uploads/2021/09/CATF_SuperhotRockGeothermal_Report.pdf.

Jones, C.G., England, K., Simmons, S., Rose, P., Mella, M., Barker, B., McLennan, J., Moore, J., 2023. Stimulation, Tracers and Geochemistry at Utah FORGE. Proceedings of the 48th Workshop on Geothermal Reservoir Engineering.

Jones, S.C., 1972. A Rapid Accurate Unsteady-State Klinkenberg Permeameter. SPE J. 12, 383–397. https://doi.org/https://doi.org/10.2118/3535-PA

Kirby, S.M., Knudsen, T., Kleber, E., Hiscock, A., 2018. Geologic Setting of the Utah FORGE Site, Based on New and Revised Geologic Mapping. GRC Transactions, Vol. 42, 2018.

Kumar, D., Ghassemi, A., 2019. Multistage Hydraulic Fracturing of EGS Wells with Application to FORGE.

Kurtoglu, B., Torcuk, M.A., Kazemi, H., 2012. Pressure Transient Analyses of Short and Long Duration Well Tests in Unconventional Reservoirs, in: All Days. SPE. https://doi.org/10.2118/162473-MS

McLaughlin, R.J., Donnelly-Nolan, J.M., 1981. Research in the Geysers-Clear Lake geothermal area, northern

California , Research in the Geysers-Clear Lake geothermal area, northern California, Geological Survey professional paper ; 1141. U.S. Department of the Interior, U.S. Geological Survey, Reston, Virginia.

McLennan, J., Mock, B., Swearingen, L., Baldwin, R., Hodder, M., Vetsak, A., Kuhns, A.T., Breland, J., 2023. Utah FORGE: Well 16B(78)-32 Drilling Data. United States. https://doi.org/https://dx.doi.org/10.15121/1998591

McLennan, J., Nash, G., Moore, J., Skowron, G., Woolsey, S., 2021. Utah FORGE - Well 16A(78)-32 Drilling Data. United States. https://doi.org/https://dx.doi.org/10.15121/1776602

Medeiros, F., Kurtoglu, B., Ozkan, E., Kazemi, H., 2007. Pressure-Transient Performances of Hydraulically Fractured Horizontal Wells in Locally and Globally Naturally Fractured Formations, in: All Days. IPTC. https://doi.org/10.2523/IPTC-11781-MS

Mindygaliyeva, Balnur, Uzun, O., Amini, K., Fleckenstein, W.W., Kazemi, H., 2023. Experimental Fracture Creation in Cores: Permeability and Porosity Measurements of the Fractured Cores and the Use of Such Measurements in Analysis of Pressure Falloff Tests Following Well Stimulation. Paper presented at the 57th U.S. Rock Mechanics/Geomechanics Symposium, Atlanta, Georgia, USA, June 2023. https://doi.org/https://doi.org/10.56952/ARMA-2023-0551

Mindygaliyeva, B., Uzun, O., Amini, K., Kazemi, H., 2023. Laboratory Measurements of Permeability and Porosity of the Matrix and Created Fractures: Application to the Pressure Falloff Analysis Following Well Stimulation to Determine Effective Fracture Spacing in Field, in: Day 1 Mon, October 16, 2023. SPE. https://doi.org/10.2118/215171-MS

Moore, J., McLennan, J., Pankow, K., Simmons, S., Podgorney, R., Wannamaker, P., Jones, C., Rickard, W., Xing, P., 2020. The Utah Frontier Observatory for Research in Geothermal Energy (FORGE): A Laboratory for Characterizing, Creating and Sustaining Enhanced Geothermal Systems. Proceedings of the 45th Workshop on Geothermal Reservoir Engineering.

Nadimi, S., Forbes, B., Moore, J., Podgorney, R., McLennan, J.D., 2020. Utah FORGE: Hydrogeothermal modeling of a granitic based discrete fracture network. Geothermics 87, 101853. https://doi.org/https://doi.org/10.1016/j.geothermics.2020.101853

Norbeck, J., Latimer, T., Gradl, C., Agarwal, S., Dadi, S., Eddy, E., Fercho, S., Lang, C., McConville, E., Titov, A., Voller, K., Woitt, M., 2023. A Review of Drilling, Completion, and Stimulation of a Horizontal Geothermal Well System in North-Central Nevada. SGP-TR-224, Proceedings , 48th Workshop on Geothermal Reservoir Engineering. Stanford University, Stanford, California, February 6-8, 2023 .

Norbeck, J.H., Latimer, T.M., 2023. Commercial-Scale Demonstration of a First-of-a-Kind Enhanced Geothermal System. (Preprint). https://doi.org/10.31223/X52X0B.

Simmons, S.F., Kirby, S., Jones, C., Moore, J., Allis, R., 2016. The Geology, Geochemistry, and Hydrology of the EGS FORGE Site, Milford Utah. Proceedings, 41st Workshop on Geothermal Reservoir Engineering, Stanford University, Stanford, CA 1181–1190.

Tester, J.W., Anderson, B.J., Batchelor, A.S., Blackwell, D.D., DiPippo, R., Drake, E.M., Garnish, J., Livesay, B., Moore, M.C., Nichols, K., Petty, S., Toksöz, M.N., Veatch Jr., R.W., 2006. The future of geothermal energy : impact of enhanced geothermal systems (EGS) on the United States in the 21st century : an assessment by an MIT-led interdisciplinary panel. MIT, Cambridge, Mass.

Titov, A., Norbeck, J., Dadi, S., Voller, K., Fercho, S., McConville, E., Woitt, M., Lang, C., Agarwal, S., Gradl, C., Latimer, T., 2023. Case Study: Completion and Well Placement Optimization Using Distributed Fiber Optic Sensing in Next-Generation Geothermal Projects, in: Proceedings of the 11th Unconventional Resources Technology Conference. American Association of Petroleum Geologists, Tulsa, OK, USA. https://doi.org/10.15530/urtec-2023-3852680

U.S. Department of Energy, O. of E.E. and R.E., 2012. Hydrothermal Resources Fact Sheet. https://www.osti.gov/biblio/1219765.

U.S. Energy Information Administration (EIA), 2023. Electricity Monthly - October 2023. https://www.eia.gov/electricity/monthly/current_month/october2023.pdf.

Wells, D., Lin, F.-C., Pankow, K., Baker, B., Bartley, J., 2022. Combining Dense Seismic Arrays and Broadband Data to Image the Subsurface Velocity Structure in Geothermally Active South-Central Utah. J Geophys Res Solid Earth 127, e2022JB024070. https://doi.org/https://doi.org/10.1029/2022JB024070

Xing, P., McLennan, J., Moore, J., 2020. In-Situ Stress Measurements at the Utah Frontier Observatory for Research in Geothermal Energy (FORGE) Site.

Energies (Basel) 13, 5842. https://doi.org/10.3390/en13215842

Zhang, S., Huang, Z., Wang, H., Zhang, H., Zhang, C., Xiong, C., 2018. Thermal characteristics analysis with local thermal non-equilibrium model during liquid nitrogen jet fracturing for HDR reservoirs. Appl Therm Eng 143, 482–492. https://doi.org/https://doi.org/10.1016/j.applthermaleng.2018.07.088

## Appendix A – FORGE Granitoid Core Data

**Table A1**. Experimental Outcomes for Granite Cores (**Fig. 3-4**) at a Net Confining Stress of 1755 psi and Pore Pressure of 245 psi.

| Core | Description | $\phi$,% | $k$,mD |
|---|---|---|---|
| GC2 | before fracturing | $\phi_m$=0.99 | $k_m$=3.68E-4 |
| GC2 | after fracturing with MTS | $\phi_t$[2]=2.07 | $k_{f,eff}$=4.16E+2 |
| GC1 | after fracturing with a saw | $\phi_t$=1.18 | $k_{f,eff}$=8.16E+2 |

**Table A2**. Porosity and permeability for FORGE horizontal core A4-9H (**Fig. 5b**) before and after fracturing.

| Data Before Fracturing | | |
|---|---|---|
| $\sigma_c$, psi | $\phi_m \cong \phi_t$, % | $k_m$, mD |
| 1255 | 0.73 | 1.09E-2 |
| 1755 | 0.73 | 7.70E-3 |
| 2755 | 0.65 | 2.73E-3 |
| 2755 | 0.61 | 2.65E-3 |
| 1755 | 0.70 | 3.68E-3 |
| 1255 | 0.76 | 7.22E-3 |
| Data After Fracturing | | |
| $\sigma_c$, psi | $\phi_t$[2], % | $k_{f,eff,core}$, mD |
| 1255 | 1.41 | 4.39E+3 |
| 1755 | 1.33 | 4.89E+3 |
| 2755 | 1.22 | 3.61E+3 |
| 2755 | 1.20 | 3.62E+3 |
| 1755 | 1.26 | 4.39E+3 |
| 1255 | 1.30 | 4.82E+3 |

**Table A3**: Porosity and permeability for FORGE vertical core A3-8V (**Fig. 6b**) before crumbling.

| Data Before Crumbling | | |
|---|---|---|
| $\sigma_c$, psi | $\phi_m$, % | $k_m$, mD |
| 1255 | 0.44 | 3.16E-4 |
| 1555 | 0.40 | 2.42E-4 |
| 1755 | 0.31 | 2.35E-4 |
| 2255 | 0.04 | 1.74E-4 |
| 2255 | 0.11 | 1.78E-4 |
| 1755 | 0.12 | 1.97E-4 |
| 1555 | 0.22 | 2.28E-4 |
| 1255 | 0.27 | 2.45E-4 |

[2] $\phi_t = \phi_{f+m} + \phi_{PVC}$

## Appendix B – Heat Transfer/Extraction Model

The Heat Transfer Model was developed to calculate heat exchange between a single hydraulic fracture connecting an injection-production pair of wells and injected water.

### Heat Transfer Governing Equations

*Hydraulic Fracture Without Leakoff:*

$$\underbrace{-\left(\rho_w c_w u_{w,f} \phi_f \frac{\partial T_f}{\partial x}\right)}_{\text{Heat Advection in HF}} \underbrace{-\left[-\left(\frac{K_y}{w_f/2}\right)\frac{\partial T_m}{\partial y}\Big|_{y=w_f/2}\right]}_{\text{Conduction of Heat at the Fracture – Matrix Interface}} = \underbrace{\phi_f \rho_w c_w + (1-\phi_f)\rho_m c_m \frac{\partial T_f}{\partial t}}_{\text{Rate of Heat Accumulatio in the Fracture}} \quad \text{(B1)}$$

*Matrix Rock:*

$$\underbrace{\frac{\partial}{\partial x}K_{m,x}\frac{\partial T}{\partial x} + \frac{\partial}{\partial y}K_{m,y}\frac{\partial T}{\partial y} + \frac{\partial}{\partial z}K_{m,z}\frac{\partial T}{\partial z}}_{\text{Heat conduction in the rock matrix surrounding fracture}} = \underbrace{\rho_s c_s \frac{\partial T}{\partial t}}_{\text{Rate of heat accumulation in the rock matrix}} \quad \text{(B2)}$$

$$u_{x,w,f}|_{x=0} = q_{inj}/(w_f h) \quad \text{(B3)}$$

### Numerical Discretization

*Hydraulic Fracture:*

$$-V_{R,i,j}\left(\rho_w c_w \underbrace{u_w \phi_f}_{v_w=\frac{q_w}{A_f}} \frac{T^{n+1}_{f,i,1}-T^{n+1}_{f,i-1,1}}{\Delta x_{i-\frac{1}{2}}}\right)+$$

$$V_{R,i,j}\left(\frac{K_m}{w_f/2}\right)\frac{T^{n+1}_{m,i,2}-T^{n+1}_{f,i,1}}{\Delta y_2/2}=$$

$$V_{R,i,j}[\phi_f\rho_w c_w+(1-\phi_f)\rho_s c_s]\frac{T^{n+1}_{f,i,1}-T^{n}_{f,i,1}}{\Delta t};$$

$$i=1,\text{Imax},j=1 \qquad \text{(B4)}$$

*Matrix:*

$$\begin{bmatrix} V_{R,i,j}\frac{K_m}{\Delta x_i}\left[\frac{T^{n+1}_{m,i+1,j,k}-T^{n+1}_{m,i,j,k}}{\Delta x_{i+1/2}}-\frac{T^{n+1}_{m,i,j,k}-T^{n+1}_{m,i-1,j,k}}{\Delta x_{i-1/2}}\right]+ \\ V_{R,i,j}\frac{K_m}{\Delta y_j}\left[\frac{T^{n+1}_{m,i,j+1,k}-T^{n+1}_{m,i,j,k}}{\Delta y_{j+1/2}}-\frac{T^{n+1}_{m,i,j,k}-T^{n+1}_{m,i,j-1,k}}{\Delta y_{j-1/2}}\right]+ \\ V_{R,i,j}\frac{K_m}{\Delta z_k}\left[\frac{T^{n+1}_{m,i,j,k+1}-T^{n+1}_{m,i,j,k}}{z_{k+1/2}}-\frac{T^{n+1}_{m,i,j,k}-T^{n+1}_{m,i,k-1}}{\Delta z_{k-1/2}}\right] \end{bmatrix} = V_{R,i,j,k}\rho_m c_m \frac{T^{n+1}_{f,i,1}-T^{n}_{f,i,1}}{\Delta t}$$

$$i=1,\text{Imax},\ j=2,JMAX,\ \ k=1,KMAX \qquad \text{(B5)}$$

Collecting appropriate terms in Eq. B4 and Eq. B5 leads to a system of linear equations which upon inversion will yield the grid temperature values at a given time step which includes the temperature in each hydraulic fracture.

$$A\vec{T}=\vec{R} \qquad \text{(B6)}$$

In the above equation $A$ is a 7-diagonal square matrix of coefficients of temperature, $\vec{T}$ the column vector of temperature values, and $\vec{R}$ column vector of residuals.

### Input Data for the Example Case Presented in the Main Body of the Paper

$\Delta x = 2.5\ ft$
$\Delta y = 2.5\ ft$
$\Delta z = h_m = 300\ ft$
$w_f = 0.04\ ft$
$\rho_w = 62.4\ \frac{lb}{ft^3}$
$\rho_m = 171.7\ \frac{lb}{ft^3}$
$\phi_f = 1$
$q_w = 1{,}200\ bbl/d$
$T_{total} = 1{,}000\ hours$
$\Delta t = 10\ hours$
$c_w = 1\ \frac{BTU}{lb°F}$
$c_m = 0.19\ \frac{BTU}{lb°F}$
$K_m = 1.763\ \frac{BTU}{fthr°F}$
$T_{initial} = 419°F = 215°C$
$IMAX = 120$
$JMAX = 60$

$$\begin{cases} for\ t = 0-49 hours;\ T_{inj} = 419°F = 215°C \\ for\ t = 50-99 hours;\ T_{inj} = 327.4°F = 164°C \\ for\ t = 100-199 hours;\ T_{inj} = 311°F = 155°C \\ for\ t = 200-599 hours;\ T_{inj} = 299.2°F = 149°C \\ for\ t = 600-1199 hours;\ T_{inj} = 284.2°F = 140°C \\ for\ t = 1200-2400 hours;\ T_{inj} = 276.2°F = 136°C \end{cases}$$

### Appendix C – Analysis of Fervo Energy's Two Pressure Falloff Data

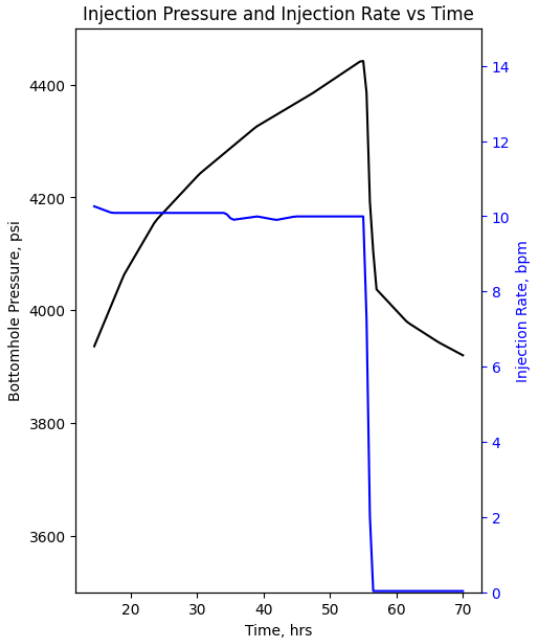


**Fig. C1.** Zoomed-in view of digitized injection data (refer to **Fig. 20**) captured just before and during the initial pressure shut-in at approximately 55 hours into the crossflow test. The production well remained shut-in for the initial ~75 hours.

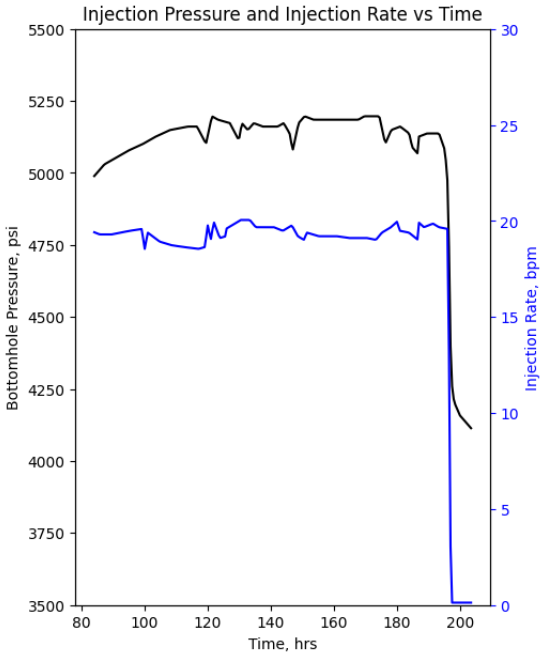


**Fig. C2.** Zoomed-in view of digitized injection data (refer to **Fig. 20**) captured just before and during the second pressure shut-in at approximately 193 hours into the crossflow test.

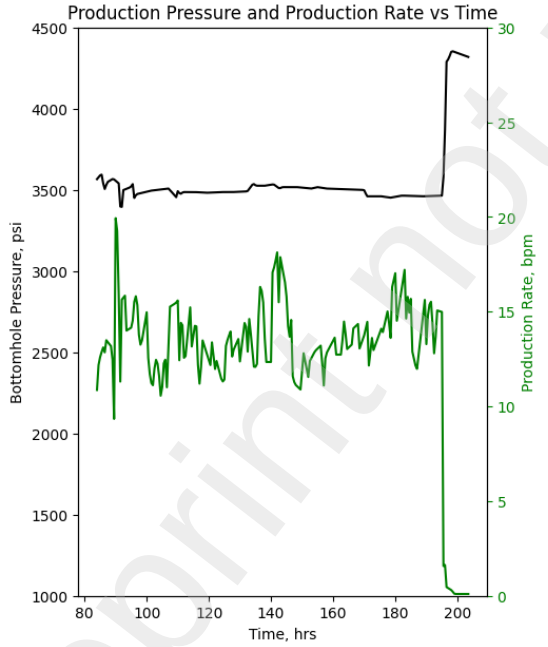


**Fig. C3.** Zoomed-in view of digitized production data (refer to **Fig. 20**) captured just before and during the second pressure shut-in at approximately 193 hours into the crossflow test.

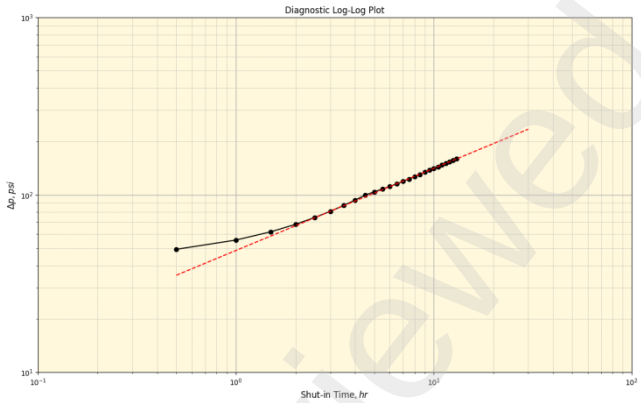


**Fig. C4.** Log-log diagnostic plot of the pressure drop (y-axis) versus shut-in time (x-axis) of the first pressure falloff case.

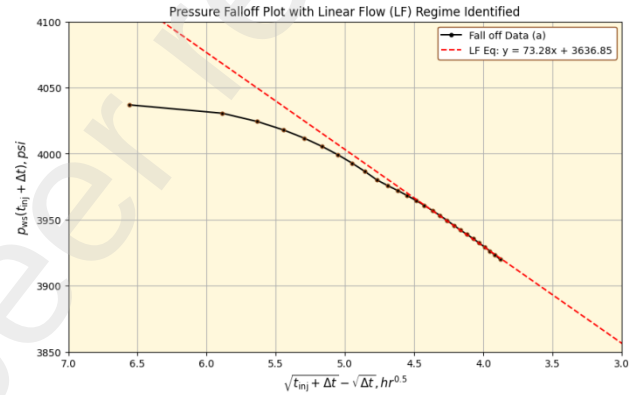


**Fig. C5.** Plot of shut-in bottomhole field pressure data (y-axis) versus the time summation (x-axis) for the first falloff.

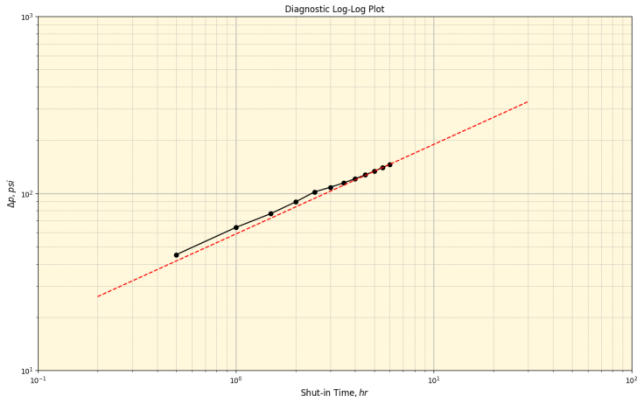


**Fig. C6.** Log-log diagnostic plot of the pressure drop (y-axis) versus shut-in time (x-axis) of the second pressure falloff case.

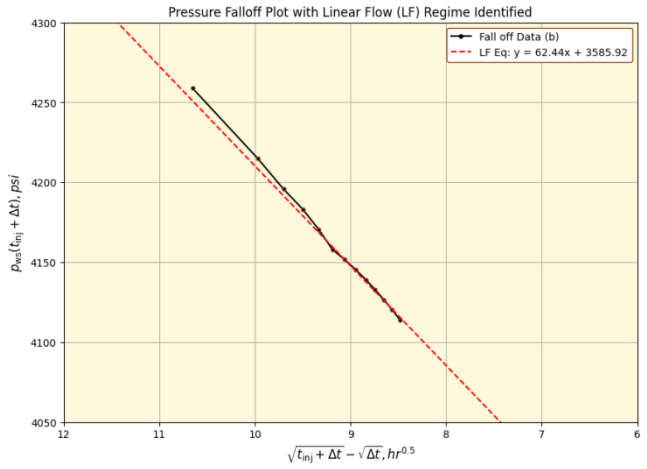


**Fig. C7.** Plot of shut-in bottomhole field pressure data (y-axis) versus the time summation (x-axis) for the second falloff.

## Appendix D– Calculation of Hydraulic Fracture Width and Permeability Using the Hydraulic Conductivity of 300 mD-feet by Fervo Energy

In the following section, we detail the formulation and computation of hydraulic fracture width ($w_{hf}$) and hydraulic fracture permeability ($k_{hf}$) based on Fervo Energy data. This involves applying Darcy's and Poiseuille's Laws. Notably, our calculations incorporate porosity and tortuosity components to accurately represent the influence of the proppant content:

*Darcy's Law, linear steady-state flow, where 0.006328 is the Darcy's Law coefficient for oil-field units. :*

$$q = -0.006328\frac{k}{\mu}A\frac{\Delta p}{\Delta L} \quad \text{(D1)}$$

*Accounting for hydraulic fracture area:*

$$q = -0.006328\frac{k_{hf}}{\mu}(n_{hf}w_{hf}h)\frac{\Delta p}{L_f} \quad \text{(D2)}$$

*Rearranging **Eq. D2** in terms of hydraulic fracture conductivity:*

$$k_{hf}w_{hf} = -\frac{1}{0.006328}\frac{q\mu L_f}{n_{hf}h\Delta p} \quad \text{(D3)}$$

The following data was used in this analysis (Norbeck and Latimer, 2023):

$q = 10\ bpm$
$h = 300\ ft$
$L_f = 365\ ft$
$\mu = 0.3\ cP$
$\Delta p = -151\ psi$ (bottomhole differential)
$n_{hf} = 100$

*Applying **Eq. D3** we get the following fracture conductivity for 100 hydraulic fractures of equal width:*

$$k_{hf}w_{hf} = -\frac{1}{0.006328}\frac{q\mu L_f}{n_{hf}h\Delta p} =$$

$$-\frac{1}{0.006328}\frac{\left(10\,\frac{bbl}{min}\times 1440\,\frac{min}{Day}\times 5.6156\,\frac{ft^3}{bbl}\right)(0.3\ cP)(365\ ft)}{(100)(300\ ft)(-151\ psi)} =$$

$$309\ mD\text{-}ft \quad \text{(D4)}$$

*Conversion of HC units from mD-ft to mD-μm:*

$$k_{hf}w_{hf} = 309\ mD\text{-}ft|_{\times 304800} =$$

$$94{,}133{,}828\ mD\text{-}\mu m \approx 9.414\times 10^7 mD\text{-}\mu m \quad \text{(D5)}$$

*Intrinsic permeability in a proppant-filled planar hydraulic fracture based on Poiseuille's Law:*

$$k_{hf} = 1.013^3\frac{w_{hf}^2\phi}{12\,\tau} \quad \text{(D6)}$$

*Combing and rearranging **Eq. D5** and **Eq. D6** to calculate hydraulic fracture width where $\frac{\phi}{\tau} = \frac{0.4}{2}$ we obtain:*

$$k_{hf} = 1.013^3\frac{w_{hf}^2\phi}{12\,\tau} = \frac{1}{w_f}9.414\times 10^7\times\frac{\phi}{\tau}\rightarrow$$

$$w_{hf}^3 = \frac{9.414\times 10^7\times 12}{1.013^3}\times\frac{\tau}{\phi}\rightarrow$$

$$w_{hf} = \sqrt[3]{\frac{9.414\times 10^7\times 12}{1.013^3}\times\frac{\tau}{\phi}} =$$

$$\sqrt[3]{\frac{9.414\times 10^7\times 12}{1.013^3}\times\frac{2}{0.4}} \approx \boxed{177\ \mu m} \quad \text{(D7)}$$

*Applying **Eq. D6** and hydraulic fracture width to calculate intrinsic fracture permeability, we obtain:*

$$k_{hf} = 1.013^3\frac{w_f^2\phi}{12\tau} = 1.013^3\,\frac{(177)^2 0.4}{12}\frac{}{2} \approx$$

$$\boxed{5.31\times 10^5 mD} \quad \text{(D8)}$$

If we use the above procedure for **50** and **20** hydraulic fractures, respectively, we obtain hydraulic fracture widths of **223** and **303** $\boldsymbol{\mu m}$, respectively.

**Observation:** (1) In the above analyses we assumed that the reported pressure differential of 151 psi was measured between injection well and production well at the same elevation. If the production well's location of pressure measurement is 100 to 150 feet shallower than the injection well, then the reported pressure differential of 151 psi must be corrected for the elevation difference in the Darcy equation which will lead to a somewhat higher hydraulic fracture conductivity.